arXiv:2205.03429v2 [cond-mat.mes-hall] 27 Aug 2024

Observation of an acoustic topological Euler insulator with meronic waves

Bin Jiang,[1,2,*] Adrien Bouhon,[3,4,†] Shi-Qiao Wu,[2,*] Ze-Lin Kong,[2]
Zhi-Kang Lin,[2] Robert-Jan Slager,[3,‡] and Jian-Hua Jiang[1,2,§]

[1] *Suzhou Institute for Advanced Research, University of Science and Technology of China, Suzhou 215123, China*
[2] *School of Physical Science and Technology & Collaborative Innovation Center of Suzhou Nano Science and Technology, Soochow University, Suzhou 215006, China*
[3] *TCM Group, Cavendish Laboratory, University of Cambridge, J. J. Thomson Avenue, Cambridge CB3 0HE, United Kingdom*
[4] *Nordita, Stockholm University and KTH Royal Institute of Technology, Hannes Alfvéns väg 12, Stockholm SE-106 91, Sweden*

(Dated: August 28, 2024)

Topological band theory has conventionally been concerned with the topology of bands around a single gap. Only recently non-Abelian topologies that thrive on involving multiple gaps were studied, unveiling a new horizon in topological physics beyond the conventional paradigm. Here, we report on the first experimental realization of a topological Euler insulator phase with unique meronic characterization in an acoustic metamaterial. We demonstrate that this topological phase has several nontrivial features: First, the system cannot be described by conventional topological band theory, but has a nontrivial Euler class that captures the unconventional geometry of the Bloch bands in the Brillouin zone. Second, we uncover in theory and probe in experiments a meronic configuration of the bulk Bloch states for the first time. Third, using a detailed symmetry analysis, we show that the topological Euler insulator evolves from a non-Abelian topological semimetal phase via the annihilation of Dirac points in pairs in one of the band gaps. With these nontrivial properties, we establish concretely an unconventional bulk-edge correspondence which is confirmed by directly measuring the edge states via pump-probe techniques. Our work thus unveils a nontrivial topological Euler insulator phase with a unique meronic pattern and paves the way as a platform for non-Abelian topological phenomena.

Introduction.— Topological phases of matter [1, 2] offer an intriguing realm with rich emergent phenomena that are unavailable in other regimes. Although the past decade has witnessed remarkable progresses in the study of topological phases [3–24], culminating in versatile classification schemes [25–29], most existing approaches by and large trace back to evaluating symmetry representations of bands in the Brillouin zone and are characterized by single gap topological invariants. Recently, a class of topological phases beyond such schemes have been steadily attracting attention [30–33]. These topological phases instead depend on the wavefunction geometry due to multi-gap conditions [30, 34]. Band degeneracies may then carry non-Abelian topological charges akin to disclinations or vortices in bi-axial nematics [35–39]. Braiding these band degeneracies can lead to novel non-trivial multi-gap topological invariants. A prototype example is the Euler class that acts as the paradigmatic real-valued analog of the Chern number [31]. Generally, such multi-gap phases can be analyzed using homotopy arguments [34] and are increasingly related to emergent physical effects and retrieved in various experimental contexts [40–43]. For instance, it was predicted that upon quenching a system with a non-trivial Euler Hamiltonian, monopole-antimonopole pairs can form in the Brillouin zone [44]. This phenomenon was recently observed in trapped-ion experiments [45]. Similarly, Euler class and non-trivial braiding was predicted in phononic systems [46–49] and electronic systems that are strained [31, 50], undergo a structural phase transition [51–53], or are submitted to an external magnetic field [54]. The most immediate playground for these uncharted topological phases of matter is, however, the metamaterials [55–60]. The non-Abelian topological charges were recently detected in one-dimensional (1D) electrical circuit metamaterials [55]. Meanwhile, in two-dimensional (2D) acoustic metamaterials, the braiding and non-Abelian topological phase transitions were demonstrated [57]. These advancements strongly indicate the promising development of this emerging field.

Here, we report the experimental realization of a topological Euler insulator phase in acoustic metamaterials which is featured with an unconventional meron (i.e., half-Skyrmion) configuration in the bulk Bloch states. Remarkably, the meron number of the bulk Bloch bands is connected to the Euler class topological index ($\chi \in \mathbb{Z}$) which is a prototype multi-gap topological invariant. We theoretically show an intricate cancellation of bulk Zak phases in the topological Euler insulator phase that permits an odd Euler class ($\chi = 1$) in this work. The cancellation of the Zak phases is then corroborated by the emergence of the in-gap edge states due to orbitals shifted to the unit-cell boundaries, revealing an unconventional bulk-edge correspondence associated with the odd Euler class topology. Using acoustic metamaterial realizations and pump-probe techniques, we manage to observe the topological Euler insulator phase by measuring the acoustic meron wave pattern in the Brillouin zone. In

addition, the Euler class topology is revealed by the in-gap edge states due to the Zak phase cancellation which are directly observed in our experiment via pump-probe detection at the edge boundaries. It is worth mentioning that in this work, the pump-probe detection is empowered by a spectral decomposition technique for the measured acoustic responses. This method not only enables us to discover the meronic acoustic wave pattern in this work, but also opens a new pathway in experimental detection of topological invariants by directly measuring the bulk Bloch wave patterns.

It is worth remarking that the observation of skyrmion and meron types of states (as well as their generalizations) in photonic and acoustic systems have inspired lots of research [61–67]. Due to the unconventional properties of these states and their potential applications in topologically robust information processing, sensing, and lasing, these states have been studied extensively recently [67]. However, to date, meronic acoustic waves have not yet been observed in experiments. Our work unveils the first observation of meronic wave patterns in acoustic systems in wavevector space, which sets a benchmark in the study of acoustic states. The unique connection between the meronic wave pattern in wavevector space and the topological Euler insulator phase also uncover intriguing physics that has not yet been revealed before.

Theoretical results.— We consider a three-band tight-binding model in 2D kagome lattice with the NN (nearest neighbor), NNN (next-to-nearest neighbor), and TNN (third nearest neighbor) couplings. There are three inequivalent lattice sites in each unit-cell, labeled separately as A, B, and C. These sites are coupled to each other via the NN, NNN, and TNN couplings which are denoted as t, t' and t'', respectively [see Fig. 1(a) and (b)]. We remark that without the TNN coupling, the system is always in various gapless semimetallic phases (as discussed thoroughly in Ref. [57]). It is crucial to introduce the TNN coupling for the emergence of the topological Euler insulator phase. In the presence of both the inversion, or effectively the 180° rotation around the z axis (C_2), and the time-reversal symmetries ($\mathcal{T}$), once a proper basis is chosen, the Hamiltonian matrix and all its eigenvectors are real-valued for arbitrary wavevector $\boldsymbol{k}$ and band index [31]. The explicit Hamiltonian matrix and the Bloch bands (including the dispersions and wavefunctions) are presented in details in the Supplemental Material [68].

We show two prototype phases in Fig. 1(c) and (d). Figure 1(c) entails a non-Abelian topological semimetalic phase with $t'' = 0$ where the three bands are interconnected. There are triple points (green dots) as the linear crossing points between the three bands (at the M and equivalent points) as well as two Dirac points (at the K and K' points, labeled by red dots) and a quadratic point (the red triangle) in the partial gap between the second and third bands. Without the TNN couplings, the topological semimetals cannot be gapped, *i.e.* , the three bands remain interconnected via various nodal points [57]. In contrast, with a finite TNN coupling t'', a nontrivial topological Euler gap can be introduced between the first and second bands [see Fig. 1(d)]. Note

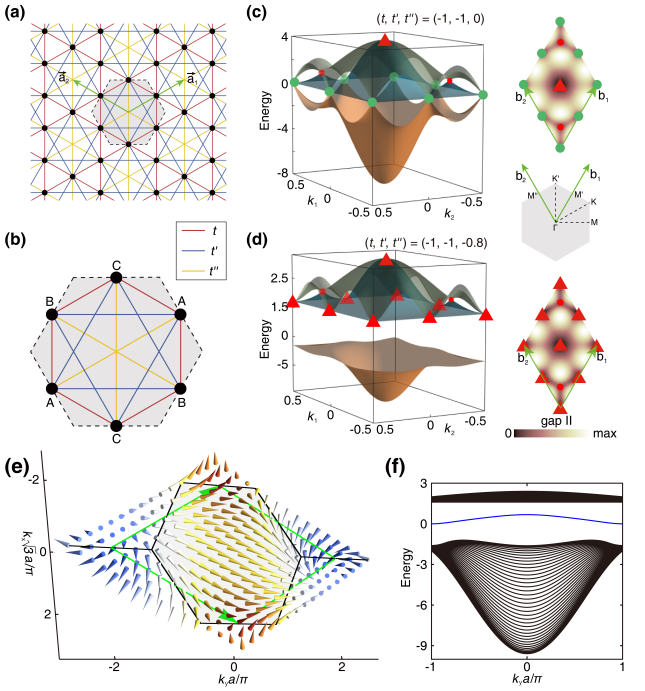


Figure 1. Theoretical results. (a) Kagome tight-binding model with unit-cell delineated by the dashed lines. The lattice vectors, $\mathbf{a}_1$ and $\mathbf{a}_2$, are denoted by green arrows. (b) The unit-cell structure. The NN, NNN, and TNN couplings are denoted as t, t' and t'', respectively (colored lines). The three inequivalent sublattice sites A, B, and C are labeled by black dots. (c) Bulk dispersion of a topological Euler semimetal with $t = t' = -1$ and $t'' = 0$. The right panels show the following: (i) the band degeneracy points between all the three bands (upper) in the rhombus Brillouin zone [linear (Dirac) crossings are represented by circles and quadratic (double) crossings by triangles] where the color map indicates the energy difference between the second and third bands, and (ii) the hexagonal Brillouin zone (lower gray hexagon) with the reciprocal primitive vectors $\boldsymbol{b}_1$ and $\boldsymbol{b}_2$ (green) chosen as the reference frame for the coordinates k_1 and k_2 [contrary to (e) that uses the k_x and k_y coordinates]. (d) The bulk dispersion of a topological Euler insulator emerges for finite t'', here with $t = t' = -1$ and $t'' = -0.8$. The right panel shows the band degeneracy points between the second and third bands in the rhombus Brillouin zone. (e) Vector distribution in the Brillouin zone (an oblique view) representing the cell-periodic part [in real space] of the Bloch wavefunction of the first band in the topological Euler insulator phase in (d). Green arrows indicate the rhombus first Brillouin zone corresponding to (c) and (d). Black lines indicate the hexagonal first Brillouin zone. (f) Energy spectrum of a supercell with the zigzag edge boundaries where the edge states in the bulk band gap are highlighted by the blue line.

that the vertical axis of Fig. 1(d) (i.e., the axis for the energy) is not uniform. The scale for the positive energy region is smaller than the scale for the negative energy region, which is designed to show the dispersion and band degeneracy points clearly for the second and third bands. These band degeneracy points are also nontrivial as will be discussed below.

The topological Euler gap is characterized by the Euler class topological index χ which in a three-band system can be expressed as follows [31, 44]

$$\chi = \frac{1}{2\pi}\int_{BZ} \mathrm{d}^2k\ \boldsymbol{n}\cdot\left(\partial_{k_x}\boldsymbol{n}\times\partial_{k_y}\boldsymbol{n}\right). \tag{1}$$

Here, the real-valued 3D unit vector $\boldsymbol{n}(\boldsymbol{k})$ is the (cell-periodic part of the) Bloch wavefunction for the first band expressed in the $\{A, B, C\}$-sublattice basis. This band topology has a number of unconventional features: First, the second and the third bands have gapless Wilson loop with nontrivial winding (see Supplemental Material [68]). This fragile crystalline topology is actually the generic nature of the split elementary band representation of the kagome lattice [28, 31, 69, 70] (see Supplementary Material [68] for more details). Second, in our system the vector representation of the first bulk band $\boldsymbol{n}(\boldsymbol{k})$ has an emergent *meron pattern* (i.e., half of a skyrmion), see Fig. 1(e) [the green arrows entail the primitive vectors of the reciprocal lattice; note that as the arrows here represent the real eigenvectors of the real Bloch Hamiltonian, they have a ±1-gauge degree of freedom. That is, if the vector is reversed, it represents the same eigenstate.]. In fact, the meron number of the Bloch eigenvector is directly connected to the Euler class $\chi = 1$ of the topological Euler insulator phase through Eq. (1) which characterizes the meronic or skyrmionic geometry of the Bloch wavefunction $\boldsymbol{n}(\boldsymbol{k})$ in the Brillouin zone (see more discussions in the Supplemental Material [68], where we show that the integrand of Eq. (1) is periodic over one rhombus Brillouin zone, while $\boldsymbol{n}(\boldsymbol{k})$ is only periodic over four rhombus Brillouin zones within which it forms two Skyrmion windings.). Third, there are two Dirac points (at K) and four quadratic points (at Γ and at M) connecting the second and the third bands which cannot be completely gapped as long as the $C_2\mathcal{T}$ symmetry is preserved. This is because these band nodes carry a nontrivial total patch Euler class 1 that forbids all of them to be annihilated together to open a band gap between the second and third bands [31, 71].

We remark that he above features are also linked to the bulk-edge response via the Zak phase. For this purpose, it is crucial to note that in our model the sublattice sites are sitting at the boundary of a unit-cell, such that the system has inherent Zak phase π even in trivial phases (i.e., the atomic limit). More precisely, in the case of a zigzag [referring to the underlying hexagonal lattice] edge termination of the kagome lattice, the perpendicular 1D chain of projected atomic sites starts and ends with atomic sites on the boundary of the 1D unit cell [a feature shared with the honeycomb (graphene) lattice when terminated by the same zigzag edge]. As a consequence and similarly to graphene, the vanishing Zak phase indicates the presence of topological edge states for the zigzag termination [72]. In the topological Euler insulator phase, the π-Zak phases along both reciprocal lattice vectors, $\boldsymbol{b}_1$ and $\boldsymbol{b}_2$ [Fig. 1(c)], are canceled by π-winding of the Bloch wavefunction due to the meronic pattern in Fig. 1(e). We stress that this is distinct from the three-band Euler insulator phases considered previously [34, 73] that are all connected to an *orientable* flag atomic limit, leading to the constraint of an *even* Euler class that must correspond to an integer multiple of skyrmions instead of merons of the bulk Bloch wavefunctions in the Brillouin zone [31, 44] which shows the profound nature from a fundamental perspective as described in the Supplemental Material [68]. Such cancellation leads to the emergence of the edge states in the topological band gap due to the vanishing Zak phase [see Fig. 1(f)]. Interestingly, in the case of an armchair edge termination, the perpendicular 1D chain of projected atomic sites now starts and ends with the site at the center of the 1D unit cell. This has the consequence to reverse the BBC of the zigzag edge, namely the vanishing Zak phase now indicates the absence of topological edge states. We actually find *two* in-gap edge states at the armchair termination which cannot be traced directly from the Zak phase [see the Supplemental Material [68]]. We emphasize that these zigzag and armchair edge state configurations are unique features of topological Euler insulators with an odd Euler class that are not found before.

Materials and methods.— To confirm the topological Euler insulator phase in experiments, we design and fabricate an air-borne acoustic metamaterial, see Fig. 2(a). The unit-cell structure is illustrated in the insets with a lattice constant $a = 36\sqrt{3}$ mm. There are three cylindrical acoustic cavities (labeled as A, B, and C), representing three sites in the unit-cell of the tight-binding model in Fig. 1. The NNN and TNN couplings are realized by tubes (with radii r_1 and r_2, respectively) connecting these cavities. Note that tubes for the NNN couplings are realized by two layers to enforce the inversion symmetry. The tubes representing TNN couplings intersect at the unit-cell center which also provide the NN couplings through indirect processes which are prominent due to the strong couplings between the acoustic cavities. By tuning the radii of these tubes, we can realize the topological Euler insulator phase in the acoustic bands. The bulk acoustic bands from both simulation and experiments are presented in Fig. 2(b). The simulation is based on solving the acoustic wave equation using commercial finite-element simulation methods (see Supplemental Material [68]). The experiments are based on acoustic pump-probe measurements. Specifically, an

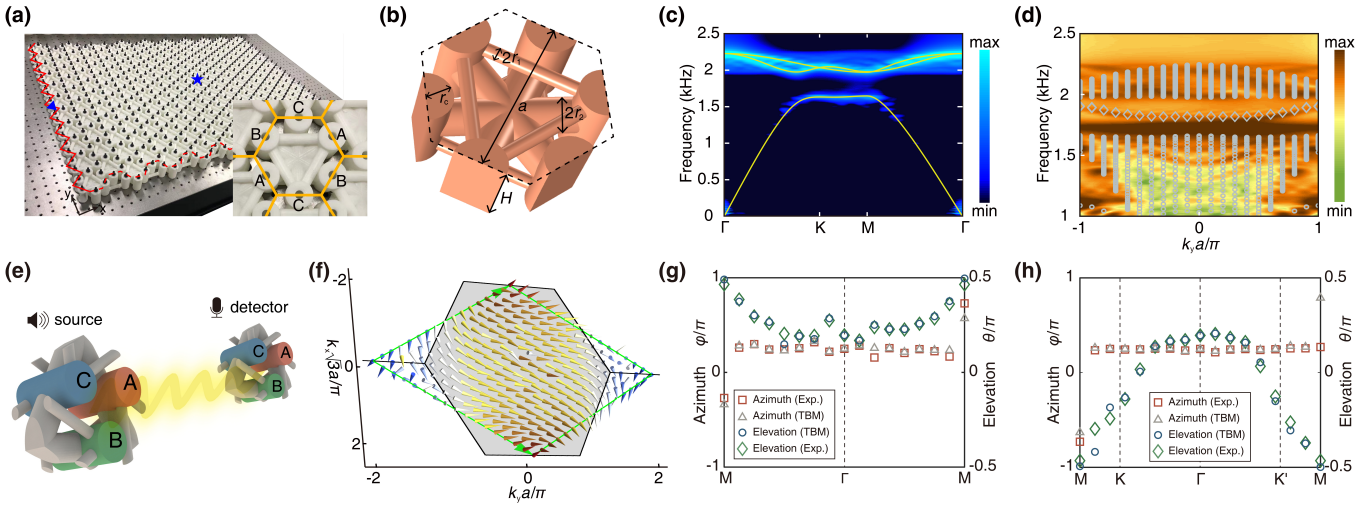


Figure 2. Experimental results. (a) Photograph of the air-borne Euler acoustic metamaterial. Inset: zoom-in photo of one unit-cell with the unit-cell boundary indicated by the yellow lines and sublattice sites labeled by the characters. (b) The structure of the air region in a unit-cell (geometric details are given in the Supplemental Material) where the unit-cell boundary is indicated by the dashed lines. (c) Acoustic bulk band structures obtained from simulation (yellow curves) and experiments (color map). (d) Measured (color map) and simulated (gray markers) dispersions of the acoustic zigzag edge states. Gray dots represent simulated bulk bands projected to the zigzag edge Brillouin zone. (e) Illustration of the pump-probe technique for the measurement of the acoustic Bloch wavefunctions. (f) The measured acoustic meron pattern, i.e., the vector Bloch wavefunctions of the first bulk band in our acoustic metamaterial (an oblique view)). Green arrows indicate the rhombus Brillouin zone as in Fig. 1(e), while black lines indicate the hexagonal Brillouin zone. (g)-(h) For the Bloch vector distribution, the variation of the azimuth and elevation angles along the (g) M-Γ-M and (h) M-K-Γ-K'-M lines are presented with the results from both the tight-binding model (TBM) and the experiments (Exp.).

acoustic source (a very small speaker) is placed in a cavity at the center of the system (indicated by the blue star) to excite the bulk Bloch acoustic waves. A detector (a small microphone) is used to scan the acoustic wavefunction in the whole system. By varying the excitation and detection frequency (they are always fixed to be equal), we obtain the acoustic wavefunctions at different frequencies. Upon Fourier transformation of the probed wavefunctions, we obtain the dispersions of the excited bulk Bloch acoustic waves.

Experimental results.— As shown in Fig. 2(c), the measured dispersion of the bulk bands agrees quite well with the acoustic bulk band structure obtained from the finite-element simulation. It is encouraging to see that the details of the second and third bands can also be reproduced in the experiments, beside the obvious band gap between the first band the remaining bands. In fact, there are two Dirac points (at the K points) and four quadratic points (three at the M points and one at Γ) between the second and the third bands. In the Supplementary Material [68], we also give the measured dispersions around these degeneracy points which also confirm the main results from the tight-binding calculations and the finite-element simulations.

Next we measure the dispersion of the acoustic edge states. By placing the acoustic source at the center of a zigzag edge [the red triangle in Fig. 2(a)], we are able to excite the edge states within the bulk band gap and measure their dispersion using similar pump-probe techniques (i.e., scanning the acoustic wavefunctions along the zigzag edge at various excitation frequencies and then performing the Fourier transformation of the detected real-space wavefunction along the edge direction). Figure 2(d) shows that the measured dispersion of the edge states is comparable with the simulated dispersion (the gray markers), confirming the emergence of the edge states in the topological Euler band gap. We note that due to the finite-size effect and the intrinsic dissipation, the valence band edge is blue-shifted and broadened. (Similarly, other bulk states are also shifted and broadened as shown in the figure.) Nevertheless, the measured dispersion of the edge states agree well with the calculated edge dispersion from finite-element simulation of the eigenstates. We emphasize again that the topological Euler phase here (as a prototype fragile topological phase protected by the $C_2\mathcal{T}$ symmetry) does not support robust gapless edge states. The observed edge states are rather due to the nontrivial Zak phase which is indirectly connected to the Euler topology in kagome lattices. As explained in details in the Supplemental Material [68], this is a unique phenomenon for odd Euler class topological phases. In fact, the Zak phase physics dominates the emergence of the edge states in this work. For instance, we find two branches of edge states for the armchair edge boundaries which stem from the evolution of

the edge states in both the complete gap I and the partial gap II due to the Zak phase under the influence of chiral symmetry breaking due to the TNN couplings (see Supplemental Material [68]). That is, one branch of the edge states comes from the partial gap II which is consistent with the observation in Ref. [57]. These phenomena enrich our understanding on the Euler topological phases.

We now reveal the most salient feature of the topological Euler gap in our acoustic system — the meron pattern in the bulk Bloch waves. For this purpose, we develop a technique of spectral decomposition based on the acoustic pump-probe measurement. The underlying principle is based on the fact that the two-points acoustic pump-probe measurement gives the two-points acoustic response function which is proportional to the retarded two-points Green's function of the acoustic waves. At a frequency of excitation and detection ν, the two-points response function is a 3×3 tensor since the source and detector can be allocated at the A, B, or C sublattice site in different pump-probe configurations. Specifically, the response function $\chi_{\alpha\beta}(\boldsymbol{r}_s, \boldsymbol{r}_d, \nu)$ is a 3×3 tensor where $\alpha, \beta = (A, B, C)$ denote the pumping and detection sites, respectively. $\boldsymbol{r}_s$ ($\boldsymbol{r}_d$) denotes the position vector of the unit-cell center that the pumping (detection) site belongs to [see illustration in Fig. 2(e)]. Upon Fourier transformation in both space and time, the measured response function becomes a function of wavevector and frequency, $\chi_{\alpha\beta}(\boldsymbol{k}, \nu)$. Theoretically, the proportionality between the response function and the retarded Green's function of acoustic waves is

$$\chi_{\alpha\beta}(\boldsymbol{k}, \nu) \propto \sum_n \frac{u^{\alpha}_{n\boldsymbol{k}}{}^* u^{\beta}_{n\boldsymbol{k}}}{\nu - (\nu_{n\boldsymbol{k}} + i\gamma_{n\boldsymbol{k}})}, \tag{2}$$

where $n = (1, 2, 3)$ is the band index, $\nu_{n\boldsymbol{k}}$ and $\gamma_{n\boldsymbol{k}}$ are, respectively, the eigenfrequency and the damping of the Bloch states of the n-th band at the wavevector $\boldsymbol{k}$. $u_{n\boldsymbol{k}}$ is the eigenvector of the Bloch states expressed in the local basis of the sublattice sites A, B, and C. To determine the Bloch eigenvector $u_{1\boldsymbol{k}}$ of the first acoustic band, we first obtain the acoustic response function $\chi_{\alpha\beta}(\boldsymbol{k}, \nu)$ through the pump-probe measurement and the Fourier transformation. We then examine the response function at the condition when the frequency is at resonance with the first acoustic bulk Bloch band, i.e., $\nu = \nu_{1\boldsymbol{k}}$, where the dominant contribution of the acoustic response function must come from the first acoustic bulk band. We use a singular value decomposition of the acoustic response function $\chi_{\alpha\beta}(\boldsymbol{k}, \nu_{1\boldsymbol{k}})$ to extract this dominant contribution. This process also gives the Bloch eigenvector $u_{1\boldsymbol{k}}$ as the eigenvector associated with the largest singular value of the acoustic response tensor $\chi_{\alpha\beta}(\boldsymbol{k}, \nu_{1\boldsymbol{k}})$ (see Supplemental Material [68] for more details). By properly tuning the overall phase factor of the eigenvector $u_{1\boldsymbol{k}}$ via the redundant gauge degree of freedom, we can map the eigenvector into a real-valued 3D unit vector $\boldsymbol{n}(\boldsymbol{k})$ which is then compared with the Bloch wavefunction of the first band in the $\{A, B, C\}$-sublattice basis calculated from the tight-binding theory.

Using this method, we observe for the first time the meron pattern in acoustic waves: Figure 2(f) gives the vector Bloch wavefunctions of the first bulk band in our acoustic metamaterial which show clearly a meron pattern in agreement with Fig. 2(a). We further check quantitatively the azimuthal and elevation angles of the measured eigenvector and the calculated eigenvector along two special lines, the M-Γ-M line [Fig. 2(g)] and the M-K-Γ-K'-M line [Fig. 2(h)]. The consistency between the experimental results and the tight-binding theory confirms the nontrivial meronic configuration of the bulk Bloch states and signifies the first observation of acoustic meron which emerges due to the topological Euler insulator phase here.

Conclusion and discussions.— Our experiments unequivocally demonstrate a unique topological Euler insulator phase in an acoustic setup with an unprecedented meronic pattern. Remarkably, the meron topological number is connected to the Euler class topological index in our kagome system. This acoustic meron pattern enriches our understanding on acoustic waves and gives an excellent example of the direct measurement of bulk topological properties. Furthermore, the observed meron pattern can be generalized to, e.g., skyrmion patterns that characterize the non-Abelian topology in systems with more bands or with an even Euler class [74]. From the experimental perspective, the discovery here may inspire future exploration of rich topological states with unconventional Bloch wavefunction patterns and thus opens a new realm for topological physics and materials.

Acknowledgements.— Jian-Hua Jiang thanks the National Key R&D Program of China (2022YFA1404400), the National Natural Science Foundation of China (Grant Nos. 12125504 and 12074281), the "Hundred Talents Program" of the Chinese Academy of Sciences, and the Priority Academic Program Development (PAPD) of Jiangsu Higher Education Institutions. Adrien Bouhon was partially funded by a Marie-Curie fellowship, grant no. 101025315 and acknowledges financial support from the Swedish Research Council (Vetenskapsradet) grant no. 2021-04681. Robert-Jan Slager acknowledges funding from a New Investigator Award, EPSRC grant EP/W00187X/1, a EPSRC ERC underwrite grant EP/X025829/1, and a Royal Society exchange grant IES/R1/221060, as well as Trinity College, Cambridge.

Author contributions.— Jian-Hua Jiang, Robert-Jan Slager, and Adrien Bouhon guided the research. Robert-Jan Slager and Adrien Bouhon established the underlying theory. Bin Jiang and Jian-Hua Jiang designed the metamaterial system and the measurement methods. Bin Jiang, Shi-Qiao Wu, Ze-Lin Kong, and Zhi-Kang Lin achieved the experimental observation and data analysis.

All authors contributed to the discussion of the results. Jian-Hua Jiang, Robert-Jan Slager, and Adrien Bouhon wrote the main text. Bin Jiang, Adrien Bouhon and Robert-Jan Slager wrote the supplementary notes.

* These authors contributed equally to this work
† Corresponding author: adrien.bouhon@su.se; These authors contributed equally to this work
‡ Corresponding author: rjs269@cam.ac.uk; These authors contributed equally to this work
§ Corresponding author: jianhuajiang@suda.edu.cn

[1] Xiao-Liang Qi and Shou-Cheng Zhang, "Topological insulators and superconductors," Rev Mod Phys **83**, 1057–1110 (2011).
[2] M. Z. Hasan and C. L. Kane, "Colloquium: Topological Insulators," Rev Mod Phys **82**, 3045–3067 (2010).
[3] Liang Fu, "Topological Crystalline Insulators," Phys Rev Lett **106**, 106802 (2011).
[4] Robert-Jan Slager, Andrej Mesaros, Vladimir Juričić, and et al., "The space group classification of topological band-insulators," Nat Phys **9**, 98 (2013).
[5] Adrien Bouhon and Manfred Sigrist, "Current inversion at the edges of a chiral p-wave superconductor," Phys Rev B **90**, 220511 (2014).
[6] Alexey A. Soluyanov and David Vanderbilt, "Smooth gauge for topological insulators," Phys Rev B **85**, 115415 (2012).
[7] Benjamin J. Wieder and B. Andrei Bernevig, "The axion insulator as a pump of fragile topology," (2018), arXiv:1810.02373.
[8] Eyal Cornfeld and Shachar Carmeli, "Tenfold topology of crystals: Unified classification of crystalline topological insulators and superconductors," Phys Rev Res **3**, 013052 (2021).
[9] Todd Van Mechelen, Sathwik Bharadwaj, Zubin Jacob, and et al., "Optical n-insulators: Topological obstructions to optical wannier functions in the atomistic susceptibility tensor," Phys Rev Res **4**, 023011 (2022).
[10] Robert-Jan Slager, Louk Rademaker, Jan Zaanen, and et al., "Impurity-bound states and green's function zeros as local signatures of topology," Phys Rev B **92**, 085126 (2015).
[11] Ari M. Turner, Yi Zhang, Roger S. K. Mong, and et al., "Quantized response and topology of magnetic insulators with inversion symmetry," Phys Rev B **85**, 165120 (2012).
[12] Benjamin Schrunk, Yevhen Kushnirenko, Brinda Kuthanazhi, and et al., "Emergence of fermi arcs due to magnetic splitting in an antiferromagnet," Nature **603**, 610–615 (2022).
[13] Robert-Jan Slager, "The translational side of topological band insulators," J Phys Chem Solids **128**, 24 – 38 (2019), spin-Orbit Coupled Materials.
[14] Toshikaze Kariyado and Robert-Jan Slager, "Selective branching and converting of topological modes," Phys Rev Res **3**, L032035 (2021).
[15] Andrej Mesaros, Robert-Jan Slager, Jan Zaanen, and et al., "Zero-energy states bound to a magnetic π-flux vortex in a two-dimensional topological insulator," Nucl Phys B **867**, 977 – 991 (2013).
[16] Ken Shiozaki and Masatoshi Sato, "Topology of crystalline insulators and superconductors," Phys Rev B **90**, 165114 (2014).
[17] Na Hyun Jo, Lin-Lin Wang, Robert-Jan Slager, Jiaqiang Yan, Yun Wu, Kyungchan Lee, Benjamin Schrunk, Ashvin Vishwanath, and Adam Kaminski, "Intrinsic axion insulating behavior in antiferromagnetic $mnbi_6te_{10}$," Phys. Rev. B **102**, 045130 (2020).
[18] Toshikaze Kariyado and Robert-Jan Slager, "π-fluxes, semimetals, and flat bands in artificial materials," Phys. Rev. Res. **1**, 032027 (2019).
[19] Robert-Jan Slager, Andrej Mesaros, Vladimir Juričić, and et al., "Interplay between electronic topology and crystal symmetry: Dislocation-line modes in topological band insulators," Phys Rev B **90**, 241403 (2014).
[20] N. P. Armitage, E. J. Mele, and Ashvin Vishwanath, "Weyl and dirac semimetals in three-dimensional solids," Rev Mod Phys **90**, 015001 (2018).
[21] Mathias S. Scheurer and Robert-Jan Slager, "Unsupervised machine learning and band topology," Phys Rev Lett **124**, 226401 (2020).
[22] Junyeong Ahn and Bohm-Jung Yang, "Symmetry representation approach to topological invariants in $C_{2z}T$-symmetric systems," Phys Rev B **99**, 235125 (2019).
[23] Jun-Won Rhim, Jens H. Bardarson, and Robert-Jan Slager, "Unified bulk-boundary correspondence for band insulators," Phys Rev B **97**, 115143 (2018).
[24] Ching-Kai Chiu, Jeffrey C. Y. Teo, Andreas P. Schnyder, and et al., "Classification of topological quantum matter with symmetries," Rev Mod Phys **88**, 035005 (2016).
[25] Jorrit Kruthoff, Jan de Boer, Jasper van Wezel, and et al., "Topological Classification of Crystalline Insulators through Band Structure Combinatorics," Phys Rev X **7**, 041069 (2017).
[26] Adrien Bouhon and Annica M. Black-Schaffer, "Global band topology of simple and double Dirac-point semimetals," Phys Rev B **95**, 241101 (2017).
[27] Hoi Chun Po, Ashvin Vishwanath, and Haruki Watanabe, "Symmetry-based indicators of band topology in the 230 space groups," Nat Commun **8**, 50 (2017).
[28] Barry Bradlyn, L. Elcoro, Jennifer Cano, and et al., "Topological quantum chemistry," Nature **547**, 298 (2017).
[29] A. Bouhon and A. M. Black-Schaffer, "Bulk topology of line-nodal structures protected by space group symmetries in class AI," ArXiv e-prints (2017), arXiv:1710.04871 [cond-mat.mtrl-sci].
[30] QuanSheng Wu, Alexey A. Soluyanov, and Tomáš Bzdušek, "Non-Abelian band topology in noninteracting metals," Science **365**, 1273–1277 (2019).
[31] Adrien Bouhon, QuanSheng Wu, Robert-Jan Slager, and et al., "Non-abelian reciprocal braiding of weyl points and its manifestation in zrte," Nat Phys **16**, 1137–1143 (2020).
[32] Junyeong Ahn, Sungjoon Park, and Bohm-Jung Yang, "Failure of Nielsen-Ninomiya Theorem and Fragile Topology in Two-Dimensional Systems with Space-Time Inversion Symmetry: Application to Twisted Bilayer Graphene at Magic Angle," Phys Rev X **9**, 021013 (2019).
[33] Y. X. Zhao and Y. Lu, "PT-Symmetric real Dirac Fermions and Semimetals," Phys Rev Lett **118**, 056401 (2017).
[34] Adrien Bouhon, Tomas Bzdusek, and Robert-Jan Slager, "Geometric approach to fragile topology beyond symmetry indicators," Phys Rev B **102**, 115135 (2020).

[35] Jaakko Nissinen, Ke Liu, Robert-Jan Slager, and et al., "Classification of point-group-symmetric orientational ordering tensors," Phys Rev E **94**, 022701 (2016).

[36] Gareth P. Alexander, Bryan Gin-ge Chen, Elisabetta A. Matsumoto, and et al., "Colloquium: Disclination loops, point defects, and all that in nematic liquid crystals," Rev Mod Phys **84**, 497–514 (2012).

[37] Ke Liu, Jaakko Nissinen, Robert-Jan Slager, and et al., "Generalized liquid crystals: Giant fluctuations and the vestigial chiral order of i, o, and t matter," Phys Rev X **6**, 041025 (2016).

[38] G. E. Volovik and V. P. Mineev, "Investigation of singularities in superfluid He^3 in liquid crystals by the homotopic topology methods," in *Basic Notions Of Condensed Matter Physics* (CRC Press, Florida, 2018) pp. 392–401.

[39] Aron J. Beekman, Jaakko Nissinen, Kai Wu, and et al., "Dual gauge field theory of quantum liquid crystals in two dimensions," Phys Rep **683**, 1 – 110 (2017), dual gauge field theory of quantum liquid crystals in two dimensions.

[40] Robert-Jan Slager, Adrien Bouhon, and F. Nur Ünal, "Non-abelian floquet braiding and anomalous dirac string phase in periodically driven systems," Nat Commun **15**, 1144 (2024).

[41] Wojciech J. Jankowski, Arthur S. Morris, Adrien Bouhon, and et al., "Optical manifestations of topological euler class in electronic materials," (2023), arXiv:2311.07545.

[42] Adrien Bouhon, Abigail Timmel, and Robert-Jan Slager, "Quantum geometry beyond projective single bands," (2023), arXiv:2303.02180.

[43] Wojciech J. Jankowski, Mohammedreza Noormandipour, Adrien Bouhon, and et al., "Disorder-induced topological quantum phase transitions in euler semimetals," (2023), arXiv:2306.13084.

[44] F. Nur Ünal, Adrien Bouhon, and Robert-Jan Slager, "Topological euler class as a dynamical observable in optical lattices," Phys Rev Lett **125**, 053601 (2020).

[45] Wending Zhao, Yan-Bin Yang, Yue Jiang, and et al., "Quantum simulation for topological euler insulators," Commun Phys **5**, 223 (2022).

[46] Bo Peng, Adrien Bouhon, Bartomeu Monserrat, and et al., "Phonons as a platform for non-abelian braiding and its manifestation in layered silicates," Nat Commun **13**, 423 (2022).

[47] Bo Peng, Adrien Bouhon, Robert-Jan Slager, and et al., "Multigap topology and non-abelian braiding of phonons from first principles," Phys Rev B **105**, 085115 (2022).

[48] Sungjoon Park, Yoonseok Hwang, Hong Chul Choi, and et al., "Topological acoustic triple point," Nat Commun **12**, 1–9 (2021).

[49] Gunnar F. Lange, Adrien Bouhon, Bartomeu Monserrat, and et al., "Topological continuum charges of acoustic phonons in two dimensions and the nambu-goldstone theorem," Phys Rev B **105**, 064301 (2022).

[50] Viktor Könye, Adrien Bouhon, Ion Cosma Fulga, and et al., "Chirality flip of weyl nodes and its manifestation in strained $mote_2$," Phys Rev Res **3**, L042017 (2021).

[51] Siyu Chen, Adrien Bouhon, Robert-Jan Slager, and et al., "Non-abelian braiding of weyl nodes via symmetry-constrained phase transitions," Phys Rev B **105**, L081117 (2022).

[52] Adrien Bouhon, Gunnar F. Lange, and Robert-Jan Slager, "Topological correspondence between magnetic space group representations and subdimensions," Phys Rev B **103**, 245127 (2021).

[53] Gunnar F. Lange, Adrien Bouhon, and Robert-Jan Slager, "Subdimensional topologies, indicators, and higher order boundary effects," Phys Rev B **103**, 195145 (2021).

[54] Yifei Guan, Adrien Bouhon, and Oleg V. Yazyev, "Landau levels of the euler class topology," (2022).

[55] Qinghua Guo, Tianshu Jiang, Ruo-Yang Zhang, and et al., "Experimental observation of non-abelian topological charges and edge states," Nature **594**, 195–200 (2021).

[56] Haedong Park, Wenlong Gao, Xiao Zhang, and et al., "Nodal lines in momentum space: topological invariants and recent realizations in photonic and other systems," (2022).

[57] Bin Jiang, Adrien Bouhon, Zhi-Kang Lin, and et al., "Experimental observation of non-abelian topological acoustic semimetals and their phase transitions," Nat Phys **17**, 1239–1246 (2021).

[58] Huahui Qiu, Qicheng Zhang, Tingzhi Liu, and et al., "Minimal non-abelian nodal braiding in ideal metamaterials," Nat Commun **14**, 1261 (2023).

[59] Haedong Park, Stephan Wong, Adrien Bouhon, and et al., "Topological phase transitions of non-abelian charged nodal lines in spring-mass systems," Phys Rev B **105**, 214108 (2022).

[60] Motohiko Ezawa, "Topological euler insulators and their electric circuit realization," Phys Rev B **103**, 205303 (2021).

[61] S. Tsesses, E. Ostrovsky, K. Cohen, and et al., "Optical skyrmion lattice in evanescent electromagnetic fields," Science **361**, 993–996 (2018).

[62] L. Du, A. Yang, A. V. Zayats, and et al., "Deep-subwavelength features of photonic skyrmions in a confined electromagnetic field with orbital angular momentum," Nat Phys **15**, 650–654 (2019).

[63] T. J. Davis, D. Janoschka, P. Dreher, and et al., "Ultrafast vector imaging of plasmonic skyrmion dynamics with deep subwavelength resolution," Science **368**, eaba6415 (2020).

[64] Cheng Guo, Meng Xiao, Yu Guo, and et al., "Meron spin textures in momentum space," Phys Rev Lett **124**, 106103 (2020).

[65] Hao Ge, Xiang-Yuan Xu, Le Liu, and et al., "Observation of acoustic skyrmions," Phys Rev Lett **127**, 144502 (2021).

[66] Biao Yang, Qinghua Guo, Dongyang Wang, and et al., "Scalar topological photonic nested meta-crystals and skyrmion surface states in the light cone continuum," Nat Mater **22**, 1203 (2023).

[67] Yijie Shen, Qiang Zhang, Peng Shi, and et al., "Optical skyrmions and other topological quasiparticles of light," Nat Photon **18**, 15 (2024).

[68] "See supplemental material at http://xxx for details." (2022).

[69] Hoi Chun Po, Haruki Watanabe, and Ashvin Vishwanath, "Fragile Topology and Wannier Obstructions," Phys Rev Lett **121**, 126402 (2018).

[70] Adrien Bouhon, Annica M. Black-Schaffer, and Robert-Jan Slager, "Wilson loop approach to fragile topology of split elementary band representations and topological crystalline insulators with time-reversal symmetry," Phys Rev B **100**, 195135 (2019).

[71] Junyeong Ahn, Dongwook Kim, Youngkuk Kim, and

et al., "Band topology and linking structure of nodal line semimetals with Z_2 monopole charges," Phys Rev Lett **121**, 106403 (2018).

[72] We remind that a Zak phase is a Berry phase computed over a non-contractible path of the Brillouin zone, *i.e.* , a path along a periodic cycle of the Brillouin zone.

[73] Tomáš Bzdušek and Manfred Sigrist, "Robust doubly charged nodal lines and nodal surfaces in centrosymmetric systems," Phys Rev B **96**, 155105 (2017).

[74] Adrien Bouhon and Robert-Jan Slager, "Multi-gap topological conversion of euler class via band-node braiding: minimal models, pt-linked nodal rings, and chiral heirs," (2022), 10.48550/ARXIV.2203.16741.

Supplementary Material for "Observation of an acoustic topological Euler insulator with meronic waves"

A. The kagome tight-binding model

B. Fragile crystalline topology

C. The "real" topology

D. From non-orientable atomic flag limit to orientable meron Euler phase

E. Design and fabrication of acoustic metamaterials

F. Numeral simulation of acoustic bulk and edges energy spectra

G. Details of acoustic bulk dispersions and their wavefunctions measurement

H. Details of the acoustic edge dispersions measurement

I. Quadratic node and Dirac points

J. Effect of defect and robustness of zigzag edge states

K. References

A. The kagome tight-binding model

We here elaborate more on the proposed model in the main text. We show that the kagome model is readily obtained from an underlying 2D hexagonal lattice of maximal symmetry. The Bravais lattice vectors of the two-dimensional primitive hexagonal lattice are chosen

$$\begin{aligned} \boldsymbol{a}_1 &= a\left(\frac{3}{2\hat{x}}+\frac{\sqrt{3}}{2\hat{y}}\right), \\ \boldsymbol{a}_2 &= a\left(-\tfrac{3}{2\hat{x}}+\tfrac{\sqrt{3}}{2\hat{y}}\right), \\ \boldsymbol{a}_3 &= \hat{z}, \end{aligned} \tag{S-1}$$

with the orthonormal Cartesian frame $\langle \hat{x}, \hat{y}, \hat{z} \rangle$, e.g., $\hat{x} = (1,0,0)$, $\hat{y} = (0,1,0)$, $\hat{z} = (0,0,1)$. Since we do not consider translations in the direction perpendicular to the basal plane ($\hat{z}$), the primitive vector $\boldsymbol{a}_3$ vector merely there to close the formula of the primitive reciprocal lattice vectors, that are given by

$$\begin{aligned} \boldsymbol{b}_1 &= 2\pi \frac{\boldsymbol{a}_2 \times \boldsymbol{a}_3}{\boldsymbol{a}_1 \cdot (\boldsymbol{a}_2 \times \boldsymbol{a}_3)}, \\ \boldsymbol{b}_2 &= 2\pi \frac{\boldsymbol{a}_3 \times \boldsymbol{a}_1}{\boldsymbol{a}_1 \cdot (\boldsymbol{a}_2 \times \boldsymbol{a}_3)}, \\ \boldsymbol{b}_3 &= 2\pi \frac{\boldsymbol{a}_1 \times \boldsymbol{a}_2}{\boldsymbol{a}_1 \cdot (\boldsymbol{a}_2 \times \boldsymbol{a}_3)}. \end{aligned}$$

Assuming that the system has the symmetry of the layer group #80, *i.e. p6/mmm* (*LG*80), with the point group D_{6h} *= 6/mmm*, the kagome lattice is then readily defined from the Wyckoff position (WP) 3*c* of *LG*80. We label {A, B, C} the sub-lattice sites of WP3*c* (*i.e.* these are three non-equivalent atomic sites in the unit cell), to which attribute the positions (see Supplementary FIG. S-1)

$$\boldsymbol{r}_A = \tfrac{\boldsymbol{a}_1}{2}, \boldsymbol{r}_B = \tfrac{\boldsymbol{a}_2}{2}, \boldsymbol{r}_C = -\tfrac{\boldsymbol{a}_1+\boldsymbol{a}_2}{2}. \tag{S-2}$$

In the following we assume that a single s-wave orbital is occupied on each sub-lattice site, and we define the site-orbital-Bloch basis by

$$|\varphi_\alpha, \boldsymbol{k}\rangle = \textstyle\sum_{\boldsymbol{R}_n} e^{i\boldsymbol{k}\cdot(\boldsymbol{R}_n+\boldsymbol{r}_\alpha)} |w_\alpha, \boldsymbol{R}_n + \boldsymbol{r}_\alpha\rangle, \tag{S-3}$$

for α = *A*, *B*, *C*, where the physical degrees-of-freedom are represented by localized Wannier functions $\langle \hat{\boldsymbol{x}} | w_\alpha, \boldsymbol{R}_n + \boldsymbol{r}_\alpha \rangle = w_\alpha(\boldsymbol{x} - \boldsymbol{R}_n + \boldsymbol{r}_\alpha)$. The Bloch Hamiltonian then takes the form

$$\mathcal{H} = \textstyle\sum_{\boldsymbol{k}} [|\varphi_A, \boldsymbol{k}\rangle\ |\varphi_B, \boldsymbol{k}\rangle\ |\varphi_C, \boldsymbol{k}\rangle] \cdot H(\boldsymbol{k}) \cdot \begin{bmatrix} \langle \varphi_A, \boldsymbol{k}| \\ \langle \varphi_B, \boldsymbol{k}| \\ \langle \varphi_C, \boldsymbol{k}| \end{bmatrix} = \textstyle\sum_{\boldsymbol{k}} |\varphi, \boldsymbol{k}\rangle\, H(\boldsymbol{k}) \langle \varphi, \boldsymbol{k}|. \tag{S-4}$$

Allowing the nearest-neighbor (NN), next-to-nearest-neighbor (NNN), and third-nearest-neighbor (TNN) hopping processes, with their corresponding tunneling amplitudes written *t*, *t'*, and *t"*, respectively (see also Supplementary FIG. S-1), we obtain the minimal kagome model tight-binding model

$$H(\boldsymbol{k}) = 2\begin{pmatrix} \epsilon_A + t''c_1''(\boldsymbol{k}) & tc_2(\boldsymbol{k}) + t'c_2'(\boldsymbol{k}) & tc_1(\boldsymbol{k}) + t'c_1'(\boldsymbol{k}) \\ tc_2(\boldsymbol{k}) + t'c_2'(\boldsymbol{k}) & \epsilon_B + t''c_2''(\boldsymbol{k}) & tc_3(\boldsymbol{k}) + t'c_3'(\boldsymbol{k}) \\ tc_1(\boldsymbol{k}) + t'c_1'(\boldsymbol{k}) & tc_3(\boldsymbol{k}) + t'c_3'(\boldsymbol{k}) & \epsilon_C + t''c_3''(\boldsymbol{k}) \end{pmatrix}, \quad \text{(S-5)}$$

where the finite Fourier terms are defined, using $c[\boldsymbol{r}](\boldsymbol{k}) = \cos(\boldsymbol{k}\cdot\boldsymbol{r})$, by $c_i(\boldsymbol{k}) = c[\boldsymbol{\delta}_i](\boldsymbol{k}), c_i'(\boldsymbol{k}) = c[\boldsymbol{\delta}_i'](\boldsymbol{k}), c_i''(\boldsymbol{k}) = c[\boldsymbol{\delta}_i''](\boldsymbol{k})$, for *i* = 1, 2, 3, with the NN bond vectors

$$\boldsymbol{\delta}_1 = -\boldsymbol{r}_B, \boldsymbol{\delta}_2 = -\boldsymbol{r}_C, \boldsymbol{\delta}_3 = -\boldsymbol{r}_A,$$

The NNN bond vectors,

$$\boldsymbol{\delta}_1' = \boldsymbol{r}_A - \boldsymbol{r}_C, \boldsymbol{\delta}_2' = \boldsymbol{r}_B - \boldsymbol{r}_A, \boldsymbol{\delta}_3' = \boldsymbol{r}_C - \boldsymbol{r}_B,$$

and finally the TNN bond vectors,

$$\boldsymbol{\delta}_1'' = \boldsymbol{a}_1, \boldsymbol{\delta}_2'' = \boldsymbol{a}_2, \boldsymbol{\delta}_3'' = -\boldsymbol{a}_1 - \boldsymbol{a}_2.$$

Let us write the momentum in units of the reciprocal lattice vectors as $\boldsymbol{k} = k_1\boldsymbol{b}_1 + k_2\boldsymbol{b}_2$, and taking $(k_1, k_2) \in [-0.5, 0.5]^2$ the domain of the Brillouin zone. The first-neighbor terms thus are

$$c_1(\boldsymbol{k}) = \cos[\pi k_2], c_2(\boldsymbol{k}) = \cos[\pi k_1], c_3(\boldsymbol{k}) = \cos[\pi(k_1 + k_2)]. \quad \text{(S-6)}$$

The second-neighbor terms are

$$c_1'(\boldsymbol{k}) = \cos[\pi(2k_1 + k_2)], c_2'(\boldsymbol{k}) = \cos[\pi(k_1 - k_2)], c_3'(\boldsymbol{k}) = \cos[\pi(k_1 + 2k_2)], \quad \text{(S-7)}$$

and the third-neighbor terms are

$$c_1''(\boldsymbol{k}) = \cos[2\pi k_1], c_2''(\boldsymbol{k}) = \cos[2\pi k_2], c_3''(\boldsymbol{k}) = \cos[2\pi(k_1 + k_2)]. \quad \text{(S-8)}$$

1. Reality condition from C_2T (PT)

The C_2T (or equivalently PT) symmetry (with $[C_2T]^2 = [PT]^2 = +1$) guaranties the existence of a choice of a Bloch-orbital basis in which the Bloch Hamiltonian matrix $H(\boldsymbol{k})$ is real [28, 30]. Since $C_{2z}T$ acts the Bloch site basis as

$$C_2T|\varphi, \boldsymbol{k}\rangle = |\varphi, m_z\boldsymbol{k}\rangle \cdot \mathbb{I}_3\mathcal{K}, \quad \text{(S-9)}$$

where $\mathbb{I}_3$ is the 3×3 identity matrix, and $\mathcal{K}$ is complex conjugation, the C_2T symmetry leads to the following constraint on the Bloch matrix $H(m_z\boldsymbol{k})^* = H(\boldsymbol{k})$ (m_z is the basal mirror symmetry), *i.e.* it must be real since $m_z\boldsymbol{k} = \boldsymbol{k}$ in the 2D Brillouin zone.

2. Spectral decomposition

The eigenvalue problem of the system is defined by the equation

$$\mathcal{H}|\psi_n, \boldsymbol{k}\rangle = E_n(\boldsymbol{k})|\psi_n, \boldsymbol{k}\rangle, \tag{S-10}$$

where $|\psi_n, \boldsymbol{k}\rangle$ is the Bloch *eigenstate* of the n-*th* eigenenergy $E_n(\boldsymbol{k})$. In the following we always assume that the eigenvalues and the corresponding eigenvectors are ordered in energy from the bottom, *i.e.* $E_1(\boldsymbol{k}) \leq E_2(\boldsymbol{k}) \leq E_3(\boldsymbol{k})$. Decomposing the Bloch eigenstates in terms of Bloch-orbital states,

$$|\psi_n, \boldsymbol{k}\rangle = \sum_{\alpha=A,B,C}|\varphi_\alpha, \boldsymbol{k}\rangle[R(\boldsymbol{k})]_{\alpha n}, \tag{S-11}$$

the eigenvalue problem reduces to

$$H_{\alpha\beta}(\boldsymbol{k})[u_n(\boldsymbol{k})]_\beta = E_n(\boldsymbol{k})[u_n(\boldsymbol{k})]_\alpha, \tag{S-12}$$

where $\{u_n(\boldsymbol{k})\}_{n=1,2,3}$ are real orthogonal Bloch *eigenvectors*. The spectral decomposition of the Bloch matrix $H(\boldsymbol{k})$ is then

$$H(\boldsymbol{k}) = R(\boldsymbol{k}) \cdot \begin{bmatrix} E_1(\boldsymbol{k}) & 0 & 0 \\ 0 & E_2(\boldsymbol{k}) & 0 \\ 0 & 0 & E_3(\boldsymbol{k}) \end{bmatrix} \cdot R(\boldsymbol{k})^T,$$

$$R(\boldsymbol{k}) = [u_1(\boldsymbol{k})\ u_2(\boldsymbol{k})\ u_3(\boldsymbol{k})] \in O(3), \tag{S-13}$$

where the diagonalizing matrix $\left[R_{\alpha n} = u_{n,\alpha}\right]_{\alpha=A,B,C;n=1,2,3}$ is composed of column Bloch eigenvectors and is orthogonal since the matrix Hamiltonian $H(\boldsymbol{k})$ is real.

3. "Orbital" Zak phases and "flag atomic limit"

We readily note that the configuration of the sub-lattice sites, in which they are shifted from the center of the unit cell and are not related via any Bravais lattice vector (this is why we call them "inequivalent"), implies the following nontrivial transformation of the Bloch matrix under a reciprocal lattice translation $\boldsymbol{K} = m\boldsymbol{b}_1 + n\boldsymbol{b}_2$ $(m, n \in \mathbb{Z})$,

$$V(\boldsymbol{K}) \cdot H(\boldsymbol{k} + \boldsymbol{K}) \cdot V(\boldsymbol{K})^\dagger = H(\boldsymbol{k}), \tag{S-14}$$

with $V(\boldsymbol{K}) = diag\left[e^{i\boldsymbol{K}\cdot\boldsymbol{r}_A}, e^{i\boldsymbol{K}\cdot\boldsymbol{r}_B}, e^{i\boldsymbol{K}\cdot\boldsymbol{r}_C}\right]$, which follows directly from the definition of Bloch basis Eq. (S-3). Then, imposing the translational symmetry of the Bloch eigenstates, *i.e.*

$$|\psi_n, \boldsymbol{k} + \boldsymbol{K}\rangle = |\psi_n, \boldsymbol{k}\rangle, \tag{S-15}$$

we get

$$u_n(\boldsymbol{k} + \boldsymbol{K}) = V(\boldsymbol{K})^T \cdot u_n(\boldsymbol{k})s_n, \tag{S-16}$$

where $s_n = \pm 1$ is a free gauge sign. The physically motivated convention to compute Berry phases along non-contractible paths across the Brillouin zone (in which case we call them Zak phases) is to use the *periodic gauge*, *i.e.* setting $s_n = 1$. We emphasize that this condition does not imply that the Bloch eigenvectors are periodic themselves. We actually show in Section D that the parallel transported vector field of $u_1(\boldsymbol{k})$ has a double period which leads to the meronic Euler topology.

It is instructive to consider a trivial limiting atomic phase of the kagome model where there is no hopping and all the bands are gapped by setting different onsite energies. (Note that this implies the breaking of the hexagonal symmetry of the system, see below.) Setting $\epsilon_A = -\epsilon_C = 1, \epsilon_B = 0,$ and $t = t' = t'' = 0$, we have

$$E_1 = \epsilon_C = -1, E_2 = \epsilon_B = 0, E_3 = \epsilon_A = 1,$$
$$[u_n]_\alpha = \delta_{n\alpha}, \tag{S-17}$$

where $\delta_{1a} = 1$ if $\epsilon_\alpha = \min_{\beta\in\{A,B,C\}} \epsilon_\beta$, $\delta_{2\alpha} = 1$ if $\epsilon_{\beta(\neq\alpha)} < \epsilon_\alpha < \epsilon_{\rho(\neq\alpha,\beta)}$, and $\delta_{3a} = 1$ if $\epsilon_\alpha = \max_{\beta\in\{A,B,C\}} \epsilon_\beta$. We can then readily derive the Berry phase (Zak phase) per band integrated along $\boldsymbol{b}_1$ and $\boldsymbol{b}_2$, noting that each band has a pure orbital composition ($\mathcal{B}_1 \equiv \mathcal{B}_C, \mathcal{B}_2 \equiv \mathcal{B}_B, \mathcal{B}_3 \equiv \mathcal{B}_A$). Writing $\gamma_{B,i}^{(\mathcal{B}_n)} = \gamma_B^{(\mathcal{B}_n)}[\Gamma + \boldsymbol{b}_i \leftarrow \Gamma]$ with $i = 1, 2$, we have

$$\begin{aligned} e^{-i\gamma_{B,i}^{(\mathcal{B}_n)}} &= u_n(\Gamma + \boldsymbol{b}_i)^T \cdot u_n(\Gamma) \\ &= u_n(\Gamma)^T \cdot V(\boldsymbol{b}_i) \cdot u_n(\Gamma) \\ &= \textstyle\sum_{\alpha,\beta} V_{\alpha\beta}(\boldsymbol{b}_i)\delta_{n\alpha}\delta_{n\beta} = e^{i\boldsymbol{b}_i\cdot\boldsymbol{r}_n}, \end{aligned} \tag{S-18}$$

and writing the vector $\gamma_B^{(\mathcal{B}_n)} = (\gamma_{B,1}^{(\mathcal{B}_n)}, \gamma_{B,2}^{(\mathcal{B}_n)})$, we find

$$\left\{\gamma_B^{(\mathcal{B}_1)} = (\pi,\pi), \gamma_B^{(\mathcal{B}_2)} = (0,\pi), \gamma_B^{(\mathcal{B}_3)} = (\pi,0)\right\} \; mod\; 2\pi. \tag{S-19}$$

In this work we call these non-zero Berry phases the *orbital* π-Zak phases, since these directly originate from the atomic off-center configuration of the orbitals in the unit cell. Indeed, we remind that the Zak phases can be interpreted as the center of localized "band" Wannier functions [S-1] (references that are not cited in the main text are listed at the end of the SI), here matching with the pure orbital degrees of freedom. Hence, we can readily verify that the π-Zak phases are in direct correspondence with the off-center locations of the orbital in the Wyckoff position 3*c* of *LG*80.

Interestingly, this completely "trivial" phase from the side of band structure (*i.e.* $H(\boldsymbol{k})$ is diagonal and has no momentum dependence), it is nevertheless non-orientable, *i.e.* it exhibits π-Berry phases along one or several non-contractible paths of the Brillouin zone torus. Such π-Zak phases imply that associated Dirac strings must cross the Brillouin zone leading to the non-trivial interaction between these and nodal points of adjacent gaps. For a detailed discussion see Ref. [30, 42, 53]. We furthermore conclude that the above phase is an atomic limit without obstruction (*i.e.* without shift of the center of the "band" Wannier orbitals as compared to the atomic orbitals) [25]. We call this atomic limit of the kagome lattice, the *flag atomic limit*, where "flag" refers to the fact that all the bands are gapped, i.e. there are two energy gaps (between bands 1 and 2, and between bands 2 and 3), such that the Bloch Hamiltonian defines a point in a flag manifold, as apposed to the gapped Euler phase that is characterized by a single energy gap such that the Bloch Hamiltonian defines a point in a Grassmannian manifold [30]. From the above example, it is straightforward to derive the Zak phases of all possible flag atomic limits, which we list in Table I.

In Section D, we discuss the intricate effect of the cancellation of the orbital Zak phases due to the presence of *band Zak phases* that now originate from nontrivial winding of the Bloch eigenvectors along non-contractible paths of the Brillouin zone. Anticipating the discussion, we find that this cancellation of Zak phases converts the non-orientable flag atomic band limit into an orientable Euler phase with a meron vector field structure (instead of a full Skyrmion).

$\varepsilon_\alpha < \varepsilon_\beta < \varepsilon_\rho$	$\gamma_B^{(\mathcal{B}_1)}$	$\gamma_B^{(\mathcal{B}_1)}$	$\gamma_B^{(\mathcal{B}_1)}$
$\varepsilon_A < \varepsilon_B < \varepsilon_C$	$(\pi, 0)$	$(0, \pi)$	(π, π)
$\varepsilon_A < \varepsilon_C < \varepsilon_B$	$(\pi, 0)$	(π, π)	$(0, \pi)$
$\varepsilon_B < \varepsilon_C < \varepsilon_A$	$(0, \pi)$	(π, π)	$(\pi, 0)$
$\varepsilon_B < \varepsilon_A < \varepsilon_C$	$(0, \pi)$	$(\pi, 0)$	(π, π)
$\varepsilon_C < \varepsilon_A < \varepsilon_B$	(π, π)	$(\pi, 0)$	$(0, \pi)$
$\varepsilon_C < \varepsilon_B < \varepsilon_A$	(π, π)	$(0, \pi)$	$(\pi, 0)$

TABLE I. Orbital Zak phase, $\gamma_B^{(\mathcal{B}_n)} = (\gamma_{B,1}^{(\mathcal{B}_n)}, \gamma_{B,2}^{(\mathcal{B}_n)})$, of the flag atomic limits of the kagome lattice. All the phases are meant to be considered mod 2π.

4. The evolutions of bulk energy spectra with the TNN coupling

In this stage, we represent the evolutions of bulk energy spectra in Eq.(S-5) with the TNN coupling. Through tuning the TNN coupling, we can trigger rich topological phase transitions in the 3-band model, as illustrated in Supplementary FIG. S-2.

During the whole tuning process, the NN and the NNN couplings are fixed to negative unit and remain unchanged. We start the tuning process with a strong and positive TNN coupling, such as t''=2. In this case, there are linear Dirac points at the K and K' points as well as a quadratic node at Γ point in gap-II and quadratic nodes at M, M' and M'' in gap-I. The Dirac nodes in gap-I have Euler class of 1/2, whereas the quadratic nodes at Γ in gap-II and at M (M' or M'') in gap-I have Euler class of 1. As shown in FIG. S2(a-c), by gradually decreasing the strength of TNN coupling but remaining positive, the rich topological phase transitions can emerge. When TNN coupling is decreased to positive unit, six Dirac nodes with Euler class of $\pm 1/2$ can be created on ΓK lines in the gap-II. Further decreasing the TNN couplings, the 6 Dirac points that are incidentally degenerate on ΓK lines are annihilated. They can be created and annihilated simultaneously due to the total of Euler class of 0.

As shown in the supplementary FIG. S-2(d), when the TNN couplings vanish, three linear triply-degenerate points with Euler class of 1/2 emerge at M, M' and M'', respectively. In following tuning process, we continuously increase the strength of the TNN coupling with negative sign. As shown in FIG. S-2(e), a gap between the first band and the second band is introduced. Specially, when the strength of the TNN coupling is negative unit, the second and the third energy bands above the gap are completely degenerate, as shown in FIG. S-2(f). The linear triply-degenerate points in FIG. S-2(d) are inevitable intermediary phase in transition of non-Abelian topological semimetals to topological Euler insulators. We emphasis that, as long as the TNN coupling is negative and finite, while we keep the other hopping parameters unchanged, the three-band model is always a topological Euler insulator.

B. Fragile crystalline topology

When $\epsilon_A = \epsilon_B = \epsilon_C$, the tight-binding model has the symmetries of hexagonal layer group *LG*80, with the point symmetry group D_{6h}. One important remark is in place here. The lattice of FIG. S-1, on which the tight-binding is based, is a slight idealization of real acoustic system on which we make the measurements. Indeed, the details of the acoustic structure (see Fig. 2(a) of the

main text) effectively breaks C_{2z} and the basal mirror symmetry m_z, while inversion I symmetry is preserved. Nevertheless, we find that the band structure of the Bloch wave functions of the acoustic wave equation for the printed structure is completely insensitive to this lowered symmetry. This actually indicates that the acoustic wavefunctions are completely insensitive to the vertical inhomogeneity of the acoustic cavities. We therefore use in the whole work the full D_{6h} symmetry, since it is the physically relevant one to characterize the band structure of the system.

1. Split EBR and symmetry-indicated winding of the two-band Wilson loop

We show in FIG. S-3 the band structure of the gapped kagome model, (t, t', t'') = (-1, -1, -0.8), along the high-symmetry lines, with the IRREPs of the symmetry group D_{6h}. The set of IRREPs of FIG. S-3 induced by the Wyckoff position 3c of LG80 constitute an elementary band representation (EBR) [25, S-2--S-7]. From of the gapping of EBR, and since the IRREPs of the two-band subspace above the gap are not compatible with any band representation of LG80 [S-8], we deduce that the gapped kagome system must host a nontrivial crystalline topology, because the two-band subspace cannot be mapped to symmetric and localized Wannier functions [25]. However, given the fact that the lower single band has no stable topology (nontrivial Euler and second Stiefel-Whitney classes require a minimum rank of 2, see below), we conclude that the system must host a fragile topology [66, 67].

The topology of the real-valued Bloch wavefunctions of the topological band gap is characterized by the Euler class $\chi \in \mathbb{Z}$, which is possible only in two-dimensional systems. This topological invariant is most conveniently obtained as the winding of the two-band Wilson loop, see FIG. S4(c). Interestingly, the data of crystal symmetries of the gapped kagome phase can be advantageously used to predict the symmetry protected winding of the Wilson loop, thus obstructing a trivial topology with no winding. This is most directly shown by considering the flow of Wilson loop over a symmetric patch that covers one sixth of the Brillouin zone, obtained by forming the path $l_{\Gamma K}$ into $l_{\Gamma M}$, see FIG. S-4(a). It was shown in Ref. [67, S-7] that the hexagonal symmetries with time reversal symmetry imposes a (minimal) finite quantized winding of the Wilson loop over the patch of $\left[\pi - \frac{2\pi}{3}\right] = \frac{\pi}{3}$ for each Wilson branch, see FIG. S4(b). This fragile

crystalline topology is actually the generic nature of the split elementary band representation of the kagome lattice [25, 67].

We have shown in Ref. [67] that the nontrivial topology of such a split EBR can be captured through the symmetry-constrained winding of (two-band) Wilson loop. Considering one patch bounded by the noncontractible paths $l_{\Gamma K}: \Gamma \to K \to \Gamma + \boldsymbol{b_1} - \boldsymbol{b}_2$ and $l_{\Gamma M}: \Gamma \to M \to \Gamma + \boldsymbol{b_1} - \boldsymbol{b}_2$, [see FIG. S-4(a)], the flow of Wilson loop upon scanning the patch by smoothly deforming $l_{\Gamma K}$ to $l_{\Gamma M}$ must be quantized. This results from the symmetry quantization of the Wilson loop phases to $\left[\frac{2\pi}{3}, -\frac{2\pi}{3}\right]$ over $l_{\Gamma K}$, and $[\pi, -\pi]$ over $l_{\Gamma M}$, see [67] for a detailed derivation. We show in FIG. S-4(b) the computed Wilson loop over the patch, obtained by deforming $l_{\Gamma K}$ (at $t = 0$) to $l_{\Gamma M}$ (at $t = 1$). Since the patch covers one sixth of the Brillouin zone, we then obtained that the two-band Wilson loop winds one time in total, *i.e.* each Wilson loop branch winds by 2π, see FIG. S-4(c).

We emphasize that while IRREPs can be used to identity a fragile crystalline topological phase coming from the splitting of an EBR, we show below that the underlying Euler topology is preserved upon the breaking of the hexagonal symmetries, while preserving C_2T (or equivalently PT), even though Wilson loop is not quantized by the unitary crystalline symmetries anymore, see FIG. S-4(d) and (e). In that sense, the Euler topology is more fundamental, similarly to the Chern topology in the complex case, and thus goes beyond the symmetry indicated topological phases [19-22, S-7].

C. The "real" topology

Given that the system satisfies time reversal symmetry (T) it belongs to the class AI of the tenfold-way of the periodic table of topological phases of matter [S-9, S-10]. In particular, the system has $C_{2z}T$ and IT symmetries that both square to the identity ($[C_{2z}T]^2 = [IT]^2 = +1$), with T the time reversal, C_{2z} the π rotation around the $\hat{z}$ axis (perpendicular to the basal plane and centered at the origin of the unit cell chosen at the center of the hexagons), and I the inversion symmetry (see the lattice in FIG. S-1, on which the model is based). The presence of an anti-unitary symmetry that squares to identity and leaves the momentum invariant implies the existence of a Bloch-orbital basis in which he matrix Hamiltonian $H(\boldsymbol{k})$ is real [28, 30]. In the case of kagome model, this real gauge is readily given by the {A, B, C}-sub-lattice site basis presented above. (In

generic cases, assuming a hermitian Hamiltonian, the real basis is obtained via Takagi factorization of symmetry unitary matrices, see the supplementary material of [47] where we present a derivation based on the singular value decomposition.) The reality condition implies that the topology of the band structure fundamentally corresponds to the topology of real vector bundles [S-11]. The $\mathbb{Z}_2$ quantization of the Berry phase in the case of real Hamiltonian directly relates to the first Stiefel-Whitney class of real vector bundles [29, 68, S-12]. This one-dimensional invariant captures the orientability of the vector bundle. Then, orientable real vector bundles of rank 2, *i.e.* with trivial first Stiefel-Whitney class, are classified by the Euler class $\chi \in \mathbb{Z}$. Any real vector bundle of higher rank, orientable or non-orientable, is classified by the reduced $\mathbb{Z}_2$ second Stiefel-Whitney class [29, 68, S-11,S-12]. Then refined and systematic homotopy classification of orientable three-band and four-band real gapped phases has been presented in Ref. [30], with the systematic derivation of minimal tight-binding models presented in Ref. [71]. We conclude this general discussion by emphasizing that the Euler (Stiefel-Whitney) class topology constitutes the basic topology of real gapped Hamiltonian, similarly to the fundamental Chern class in complex case.

As shown in FIG. S-4(d), the total winding of Wilson loop, which indicates the non-zero Euler class [29, 30, 67, 68, 70], upon the breaking of the hexagonal symmetries (and preserving C_2T) leading to the absence of quantization of Wilson loop over special symmetric paths (c), shows that the Euler topology goes beyond the framework of symmetry-indicated topologies. See Ref. [30] and [71] with plenty of examples of models with a variety of difference Euler phases that are not indicated by symmetry.

The topology of a real orientable 1 + 2-gapped three-band system, *i.e.* $E_1(\boldsymbol{k}) < E_2(\boldsymbol{k}) \leq E_3(\boldsymbol{k})$, is classified by Euler class [28, 29, 68, 71]

$$\chi = \frac{1}{2\pi}\int_{BZ}\left[\partial_{k_x}u_2\partial_{k_y}u_3 - \partial_{k_y}u_2\partial_{k_x}u_3\right]dk_x \wedge dk_y,$$
$$= \tfrac{1}{2\pi}\textstyle\int_{BZ} u_1(\boldsymbol{k})\cdot\left[\partial_{k_x}u_1(\boldsymbol{k})\times\partial_{k_y}u_1(\boldsymbol{k})\right]dk_xdk_y \in (2)\mathbb{Z}, \qquad \text{(S-20)}$$

where we note the prefactor $\frac{1}{2\pi}$ in front of the Skyrmion number (instead of the usual prefactor $\frac{1}{4\pi}$), leading to the doubling of the Euler class whenever the vector field $u_1(\boldsymbol{k})$ winds fully over the unit sphere, *i.e.* forming a Skyrmion vector field. In the next Section, we discuss the winding of

the vector field $u_1(\boldsymbol{k})$ and show that gapped kagome phase hosts a nontrivial Euler phase, with the caveat that $u_1(\boldsymbol{k})$ winds only as meron instead of a full skyrmion.

D. From non-orientable atomic flag limit to orientable meron Euler phase

We have noted in Supplementary Material A 3 that atomic limit of the kagome lattice is non-orientable, *i.e.* with π-Zak phases, due to the off-centered location of the atomic orbitals. We present in the main text the Euler topology of the gapped kagome. In principle, however, the Euler class is not defined in non-orientable phases (as it is not defined for non-orientable real vector bundles, *i.e.* hosting nontrivial first Stiefel-Whitney class). We here resolve this apparent contradiction.

The vector field of first Bloch eigenvector $u_1(\boldsymbol{k})$ of the gapped kagome phase, shown in Fig. 1(e) of the main text, clearly shows the presence of π-winding across non-contractible paths of the Brillouin zone. This is very clear for instance along the path $\left[\Gamma - \frac{\boldsymbol{b}_1}{2} - \frac{\boldsymbol{b}_2}{2} \to \Gamma + \frac{\boldsymbol{b}_1}{2} - \frac{\boldsymbol{b}_2}{2}\right] = \left\{\boldsymbol{k}\middle| k_2 = \pm\frac{1}{2}, k_1 \in \left[-\frac{\frac{1}{2,1}}{2}\right]\right\}$ connecting the three inequivalent M points: in Fig. 1(e) the arrow is blue when pointing downwards and red when pointing upwards.

In order to show this, let us first discuss the general structure of the Wilson loop along a non-contractible path of the Brillouin zone. The Wilson loop for n_{occ} occupied real Bloch eigenvectors, *i.e.* forming the rectangular matrix $R_{occ}(\boldsymbol{k}) = \left[u_1(\boldsymbol{k}) \dots u_{n_{occ}}(\boldsymbol{k})\right]$ which we call a *sub-frame*, can be defined as

$$\mathcal{W}_{\boldsymbol{k}_0}[\boldsymbol{K}] = R^p_{occ}(\boldsymbol{k}_0 + \boldsymbol{K})^T \cdot \tilde{R}_{occ}(\boldsymbol{k}_0 + \boldsymbol{K}) \cdot \left[\tilde{R}_{occ}(\boldsymbol{k}_0 + \boldsymbol{K})^T \cdot \left(\prod_{\boldsymbol{k}}^{\boldsymbol{k}_0+\boldsymbol{K}\leftarrow\boldsymbol{k}_0} \tilde{P}_{\boldsymbol{k}}\right) \cdot R_{occ}(\boldsymbol{k}_0)\right],$$
$$= R_{occ}(\boldsymbol{k}_0)^T \cdot V(\boldsymbol{K}) \cdot \tilde{R}_{occ}(\boldsymbol{k}_0 + \boldsymbol{K}) \cdot \widetilde{\mathcal{W}}_{\boldsymbol{k}_0}[\boldsymbol{K}], \quad \text{(S-21)}$$

where the index 'p' refers to the periodic gauge, *i.e.* we used (see Supplementary Material A 3)

$$R^p_{occ}(\boldsymbol{k}_0 + \boldsymbol{K}) = V(\boldsymbol{K})^T \cdot R_{occ}(\boldsymbol{k}_0), \quad \text{(S-22)}$$

and the tilde refers to parallel transported quantities, such as the sub-frame $\tilde{R}_{occ}(\boldsymbol{k})$ and projector $\tilde{\mathcal{P}}_{\boldsymbol{k}} = \tilde{R}_{occ}(\boldsymbol{k}) \cdot \tilde{R}_{occ}(\boldsymbol{k})^T$. We then get the Berry phase by taking the determinant, *i.e.*

$$e^{-i\gamma_B[\boldsymbol{K}]} = det\mathcal{W}_{\boldsymbol{k}_0}[\boldsymbol{K}],$$
$$= \det\{R_{occ}(\boldsymbol{k}_0)^T \cdot V(\boldsymbol{K}) \cdot \tilde{R}_{occ}(\boldsymbol{k}_0 + \boldsymbol{K})\}, \quad \text{(S-23)}$$

where we have used that the Berry phase of the parallel transported real Bloch eigenvectors is identically zero, *i.e.*

$$det\widetilde{\mathcal{W}}_{\boldsymbol{k}_0}[\boldsymbol{K}] = e^{-i\tilde{\gamma}_B[\boldsymbol{K}]} = 0. \tag{S-24}$$

Applying Eq. (S-23) to the first Bloch eigenvector of the system, *i.e.* $R_{\text{occ}} = u_1$, we get

$$e^{-i\gamma_B^{(B_1)}[\boldsymbol{K}]} = u_1(\boldsymbol{k}_0)^T \cdot V(\boldsymbol{K}) \cdot \tilde{u}_1(\boldsymbol{k}_0 + \boldsymbol{K}). \tag{S-25}$$

Since in a flag atomic limit we have $[\tilde{u}_1(\boldsymbol{k})]_\alpha = [u_1(\boldsymbol{k}_0)]_\alpha = \delta_{1\alpha}$, we recover the results of Table I in Supplementary Material A 3. Considering the example with $\epsilon_C < \epsilon_B < \epsilon_A$ (see Supplementary Material A 3), we get $\left(\gamma_B^{(B_1)}[\boldsymbol{b}_1], \gamma_B^{(B_1)}[\boldsymbol{b}_2]\right) = (\pi, \pi)$.

Let us now consider the gapped Euler phase with the parallel transported vector field of Fig. 1(e) of the main text. Setting $\boldsymbol{k}_0 = -\frac{\boldsymbol{b}_1}{2} - \frac{\boldsymbol{b}_2}{2} = M - \boldsymbol{b}_1$ and $\boldsymbol{K} = \boldsymbol{b}_1$ [see FIG. S-4(a)], we find from parallel transported profile

$$\tilde{u}_1(M) = -u_1(M - \boldsymbol{b}_1) = (0,0,1)^T, \tag{S-26}$$

from which we get

$$\begin{aligned} e^{-i\gamma_B^{(B_1)}[\boldsymbol{b}_1]} &= u_1(M - \boldsymbol{b}_1)^T \cdot V(\boldsymbol{b}_1) \cdot \tilde{u}_1(M) \\ &= (0,0,1)diag[-1,1,-1](0,0,-1)^T \\ &= +1, \end{aligned} \tag{S-27}$$

from which we conclude $\gamma_B^{(B_1)}[\boldsymbol{b}_1] = 0 \mod 2\pi$. A similar computation, integrating the Zak phase along $\boldsymbol{b}_2$ instead, we get $\gamma_B^{(B_1)}[\boldsymbol{b}_2] = 0 \mod 2\pi$.

Comparing the Zak phases of the flat atomic limit with the Zak phase of the gapped Euler phase, we thus conclude that the π-orbital Zak phases are compensated by π-Zak phases coming from the winding of the Bloch eigenvectors. We thus call the later the *band Zak phase*. All in all, the cancellation of Zak phases results in an effectively orientable phase, *i.e.* with zero Berry phase, or equivalently, with trivial first Stiefel-Whitney class. As a consequence, the (two-dimensional) Euler class is naturally well defined. One very interesting consequence is that the Euler class of the gapped kagome phase is $\chi = 1$, *i.e.* it is *odd*. This must be contrasted with the result that every three-band system that hosts an orientable flag atomic limit only allows nontrivial Euler phases with an *even* Euler class (thus the factor (2) in front of $\mathbb{Z}$ in Eq. (S-20)) [30, 71].

Let us elaborate further. The flattened Hamiltonian of any 1 + 2-three-band system is (taking the eigenvalues to be $E_1 = -E_2 = E_3 = 1$) [28, 70]

$$H(k) \to Q(k) = 2u_1(\boldsymbol{k}) \cdot u_1(\boldsymbol{k})^T - \mathbb{I}_3. \tag{S-28}$$

Because of the quadratic dependence on u_1, whenever the vector u_1 winds fully over the unit sphere a number N of times, the Euler class is $2N$, via Eq. (S-20). We thus conclude that an odd Euler class of 1, as found in the gapped kagome phase should be associated with a winding by a half-Skyrmion, that is a meron winding. We prove this more rigorously below.

1. Proof of the quantized meron winding

In this section, we prove that the gapped Euler phase with $\chi = 1$ originates from the meron winding of one of its Bloch eigenvectors.

Since $V(2\boldsymbol{b}_1) = V(2\boldsymbol{b}_2) = \mathbb{I}$, we know that $u_1(\boldsymbol{k})$ must be periodic, up to a gauge sign, over a rhombus spanned by $2\boldsymbol{b}_1$ and $2\boldsymbol{b}_2$. Taking the parallel transported vector field of $u_1(\boldsymbol{k})$, i.e. obtained by fixing the space dependent gauge sign of $u_1(\boldsymbol{k})$ such that it is continuous, we indeed show in FIG. S-5 that it is periodic over *four* rhombus Brillouin zones (that is the surface inside the red diamond). We also see very clearly that the quadruple Brillouin zone contains *two* Skyrmion windings. We infer that *one* meron winding is realized by the vector field over a *single* rhombus Brillouin zone (green diagmond). It can actually be rigorously established that the quantization of the odd Euler class is indeed associated with a meronic pattern. To show this, we first note the symmetry of the Bloch Hamiltonian under C_{2z} (I) symmetry (represented by an identity matrix), i.e. $H(-\boldsymbol{k}) = H(\boldsymbol{k})$, which implies that the Bloch eigenvectors can be taken symmetric under C_{2z} symmetry, i.e. $u_1(-\boldsymbol{k}) = u_1(\boldsymbol{k})$. This agrees with the parallel transported vector field in FIG. S-5.

As a consequence of its inversion symmetry, $u_1(\boldsymbol{k})$ can be split into two identical parts defined on distinct halves (images of one another under inversion) of the Brillouin zone. More precisely, we represent $u_1(\boldsymbol{k})$ (scanning over a single rhombus Brillouin zone) over a unit sphere in FIG. S-6 and decompose it into its two overlapping parts: in FIG. S-6(a), we plot $u_1(\boldsymbol{k})$ over one-half of the rhombus Brillouin zone $k_1 \in [-0.5,0.5]$ and $k_2 \in [-0.5,0.]$ (blue points); In FIG. S-6(a), we plot $u_1(\boldsymbol{k})$ the other half $k_1 \in [-0.5,0.5]$ and $k_2 \in [0.,0.5]$ (red points). It is crucial that each part covers exactly one half of an hemisphere. We emphasize that this data confirms the symmetry of $u_1(\boldsymbol{k})$ under inversion.

Making use of the inversion symmetry of the vector field, one can simplify the computation of the Euler class. Writing the integrand $I(\boldsymbol{k}) = u_1(\boldsymbol{k}) \cdot \left[\partial_{k_x} u_1(\boldsymbol{k}) \times \partial_{k_y} u_1(\boldsymbol{k})\right]$, we split the Euler class formula as

$$\chi = \chi_{1/2} + \chi_{2/2},$$

with

$$\chi_{1/2} = \int_{-0.5}^{0.5} dk_x \int_{-0.5}^{0.} dk_y \, I(\boldsymbol{k}),$$

and

$$\chi_{2/2} = \int_{-0.5}^{0.5} dk_x \int_{0.}^{0.5} dk_y \, I(\boldsymbol{k}).$$

Then, changing the variable to $\boldsymbol{k}' = -\boldsymbol{k}$, we find

$$\begin{aligned}\chi_{1/2} &= \int_{0.5}^{-0.5} d(-k'_x) \int_{0.5}^{0.} d(-k'_y) \, I(-\boldsymbol{k}') = \int_{0.5}^{-0.5} dk'_x \int_{0.5}^{0.} dk'_y \, I(\boldsymbol{k}'), \\ &= \int_{-0.5}^{0.5} dk'_x \int_{0.}^{0.5} dk'_y \, I(\boldsymbol{k}'), \\ &= \chi_{2/2},\end{aligned}$$

where we have used $I(-\boldsymbol{k}') = I(\boldsymbol{k}')$, itself following from $u_1(-\boldsymbol{k}) = u_1(\boldsymbol{k})$. We finally conclude that

$$\chi = 2\chi_{1/2}.$$

Since $u_1(\boldsymbol{k})$ is covering one half hemisphere by scanning $\boldsymbol{k}$ over one half of the rhombus Brillouin zone [FIG. S-6], we find $\chi_{1/2} = 1/2$, and thus $\chi = 1$.

We finally conclude that there are two classes of three-band systems with Euler topology. On one hand, the systems that host an orientable flag atomic limit give rise to Euler phases with an even Euler class. We called these the *Skyrmionic Euler phases*. On the other hand, the systems that host a non-orientable flag atomic limit give rise to Euler phases with an odd Euler class. We call these the *meronic Euler phases*.

E. Design and fabrication of acoustic metamaterials

To reproduce salient topological properties in tight-binding model, we design a type of acoustic kagome metamaterial, based on coupled acoustic resonators to verify the Euler insulators in experiment. In our design, the A, B, and C sites are realized by three identical cylinder acoustic resonators, whose geometry paraments are the same, with height H = 36mm and radii r_c = 9.6mm.

And the NN, NNN and TNN couplings are realized by two types of horizontal tubes. Those thicker tubes connecting the TNN resonators with radii r_2 = 7.0mm, mainly contribute TNN couplings, at the distance H/2 from both the top or bottom surfaces. They intersect at the center of the unit-cell, so that they can partly produce NN as well as slight NNN couplings in an indirect way. To compensate the strengths of the NNN couplings to be close to NN couplings, the rest of thin tubes connect the NNN resonators with radii r_1 = 2.7mm, at the distance H/6 from the top or bottom surfaces. Such a design with two layers of NNN coupled tubes efficiently avoids crossing with each other. We remark that, the coupling strengths depend only on the radii and length of the tubes, and independent of the position of the tubes. The lattice constant here is $a = 36\sqrt{3}$ mm, and all geometry paraments are summarized in FIG. S-7(b).

The air region is encapsulated by a shell of photosensitive resin with thickness about 1.8mm, which imprison acoustic waves. To perfectly match with rubber plugs and enhance the structural stability of metamaterials, the upper and lower resin layers are enhanced to 3mm. Meanwhile, the top hole with diameter 7mm is convenient to manually detect acoustic signals as well as insert acoustic source into a resonator for acoustic excitation.

Recently, the development of 3D printing technology has been more and more mature, which provide a feasible avenue to manufacture acoustic metamaterials. By virtue of this technology, the two experimental samples [one given in Fig. 2(a) in the main text and another in Supplementary FIG. S-10(a)] were well fabricated in a commercial company in Shenzhen city, at precision within 0.1mm. Both samples are constructed with the unit element in FIG. S-7(a). The sample given in Fig. 2(a) in the main text has 200 unit-cells and dimension of 1050mm*710mm*42mm along the x, y and z directions, respectively. The lower boundary (marked by solid lines) is sealed, showing an armchair edge, while other three half-opened boundaries (left boundary marked by dashed lines) lead to acoustic wave leaking out into free space. Such a design is beneficial for experimental measurements of acoustic Bloch states (for example, bulk dispersions and acoustic Bloch eigenstates) and projected armchair edge states dispersions. Another sample given in Supplementary FIG. S-10(a) owns more than 215 unit-cells and dimension of 620mm*1270mm*42mm along the x, y and z directions, respectively. Compared with the first sample, another sample, along y (or zigzag boundary) direction lengthened, is used specifically to detect zigzag edge dispersions. The closed zigzag boundary yields zigzag edge states, while other

three boundaries are half-opened. In our set-up, the zigzag (armchair) boundary is along y (x) direction.

F. Numeral simulations of acoustic bulk and edges energy spectra

All numeral simulations of acoustic energy bands or dispersions are performed using the commercial finite-element solver package COMSOL Multiphysics 5.5 version. The photosensitive resin used in 3D printing can be regard as rigid wall, because of huge acoustic impendence mismatch with air background. The inner space is filled with air (at room temperature, with a mass density of $1.3 kgm^{-3}$ and sound speed of $343 ms^{-1}$.). The bulk dispersions can be calculated through solving eigen-value equation for acoustic waves in a unit-cell with periodic boundary conditions in 2D x-y plane. And the edge dispersions also can be calculated through solving the same equation in ribbon-like structures with armchair or zigzag boundary in one direction and periodic boundary condition in the other.

G. Details of acoustic bulk dispersions and their wavefunctions measurement

A speaker as an acoustic source is inserted into a resonator in the center of the sample through the top hole for excitation of bulk states. To capture acoustic signals more accurately, the probe microphone is connected to a power amplifier with 10 times amplification. We keep all holes by rubber plugs except two resonators with the speaker and probe microphone. The excited acoustic signals are then detected manually in each resonator using the probe microphone. With the assistance of the Aglient network analyzer (Key Words E5061B), we record the acoustic complex-valued wavefunction at each excitation frequency ranging from 5Hz to 3kHz. Technologically, the detected signal is the acoustic pressure in each resonator with both amplitude and phase signals. Therefore, for each excitation frequency, we obtain a profile of the detected acoustic field. Some examples of the detected acoustic pressure profiles are shown in FIG. S-8(a-c). Note that the measured acoustic field profiles under the same excitation frequency are different when the acoustic source (labeled as the blue star in the figures) is placed in the A, B or C sites in the same unit cell, since in kagome lattices, these sites are inequivalent.

We performer the measurements with source placed at A, B and C sites in the central unit cell. The three measurements are independent. We then carry out the 2D discretized Fourier

transformation of the detected acoustic pressure profiles on the A, B and C sub-lattice. In another words, at an excitation frequency *f*, from detected real space acoustic pressure signals, or two-points Green's function of acoustic waves $\chi_{\beta\alpha}(\boldsymbol{r}_s, \boldsymbol{r}_d, f)$ where $\boldsymbol{r}_s(\boldsymbol{r}_d)$ denotes the position vector of the source (detector), we obtain a Fourier transformed 3*3 response function $\chi_{\beta\alpha}(\boldsymbol{k}, f)$ with index α, β = (A, B, C) denotes the pumping and detection sites, respectively. For a given wavevector $\boldsymbol{k}$ at an excitation frequency *f*, the 3*3 response function tensor is derived from additional contributions where all Bloch acoustic wavefunctions are integrated over the whole space,

$$\chi_{\beta\alpha}(\boldsymbol{k}, f) \sim \sum_n \int d\boldsymbol{r}_d \frac{e^{-i\boldsymbol{k}\cdot\boldsymbol{r}_d}\psi_\beta(\boldsymbol{r}_d)\psi^*_\alpha(\boldsymbol{r}_s)}{f-(f_{n\boldsymbol{k}}+i\gamma_{n\boldsymbol{k}})}, \tag{S-29}$$

where n (= 1, 2, 3) is the band index, $f_{n\boldsymbol{k}}$ and $\gamma_{n\boldsymbol{k}}$ are the eigenfrequency and the damping of the Bloch states of of the *n*-th band at the wavevector $\boldsymbol{k}$. $u_{n\boldsymbol{k}}$ is the eigenvector of the Bloch states of n-th band at wavevector $\boldsymbol{k}$ written in local basis of the sublattice sites A, B, and C.

For the sake of simplification, we take the position of the acoustic source as the origin of the coordination. Through substituting $\psi_\alpha(\boldsymbol{r}_s = \boldsymbol{0}) = \Sigma_{\mathbf{q}} u^\alpha_{n\boldsymbol{q}}$ and $\psi_\beta(\boldsymbol{r}_d) = \Sigma_{\mathbf{q}} e^{i\boldsymbol{q}\cdot\boldsymbol{r}} u^\beta_{n\boldsymbol{q}}$ in Eq. (S-29) and simultaneously utilizing Bloch theory $\psi_{n\boldsymbol{q}} = e^{i\boldsymbol{q}\cdot\boldsymbol{r}} u_{n\boldsymbol{q}}$, We obtain, theoretically,

$$\chi_{\beta\alpha}(\boldsymbol{k}, f) \sim \sum_n \frac{u^\beta_{n\boldsymbol{k}} {u^\alpha_{n\boldsymbol{k}}}^*}{f-(f_{n\boldsymbol{k}}+i\gamma_{n\boldsymbol{k}})}. \tag{S-30}$$

To carefully check the experimental acoustic bulk dispersions, we sum the intensity of three Fourier transformed acoustic signals together,

$$P_\alpha(\boldsymbol{k}, f) = \sum_\beta \chi^*_{\beta\alpha}(\boldsymbol{k}, f)\chi_{\beta\alpha}(\boldsymbol{k}, f). \tag{S-31}$$

The quantity $P_\alpha(\boldsymbol{k}, f)$ is presented in supplementary FIG. S-8(d-f). Specially, we present the obtained $P_\alpha(\boldsymbol{k}, f)$ for three different positions with the source in site A [FIG. S-8(d)], B [FIG. S-8(e)] and C [FIG. S-8(f)] in the central unit cell. The bulk dispersions of three independent measurements are slightly different essentially due to the fact that A, B, and C sites are inequivalent in kagome lattices. The obtained $P_{\alpha=A}(\boldsymbol{k}, f)$ in FIG. S-8(d) is selected into Fig. 2(c) in the main text as an experimental example of bulk dispersions.

To measure the acoustic Bloch eigenstates $u_{1\boldsymbol{k}}$, we examinate the response function at resonance with the first acoustic band, $f = f_{1\boldsymbol{k}}$, where the dominant contribution in Eq. (S-30) from the first band. We then carry out a singular value decomposition of the response function tensor,

$$\chi_{\beta\alpha}(\boldsymbol{k}, f_{1\boldsymbol{k}}) = U(\boldsymbol{k}, f_{1\boldsymbol{k}})\Sigma(\boldsymbol{k}, f_{1\boldsymbol{k}})V^{\dagger}(\boldsymbol{k}, f_{1\boldsymbol{k}}). \quad \text{(S-32)}$$

The column of $U(\boldsymbol{k}, f_{1\boldsymbol{k}})$ corresponding to the maximum absolute value of eigenvalue of the response function matrix encodes the crucial Bloch eigenstates $u_{1\boldsymbol{k}}$. We remark that, if we switch the pumping and detection sites, which is equivalent to transpose the response function tensor, the information of Bloch eigenstates will include in the matrix $V(\boldsymbol{k}, f_{1\boldsymbol{k}})$. By properly tuning the overall phase factor of $u_{1\boldsymbol{k}}$,

$$u_{1\boldsymbol{k}} = \begin{pmatrix} u_{A1} \\ u_{B1} \\ u_{C1} \end{pmatrix} = \begin{pmatrix} \rho_A e^{i\theta_A} \\ \rho_B e^{i\theta_B} \\ \rho_C e^{i\theta_C} \end{pmatrix} \rightarrow n'(\boldsymbol{k}) = Re\left[e^{-i\bar{\theta}} \begin{pmatrix} u_{A1} \\ u_{B1} \\ u_{C1} \end{pmatrix}\right], \quad \text{(S-33)}$$

where $\bar{\theta} = \frac{\rho_A\theta_A+\rho_B\theta_B+\rho_C\theta_C}{\rho_A+\rho_B+\rho_C}$, we can map it to a three-dimensional real-valued unit vector $n(\boldsymbol{k}) = \frac{n'(\boldsymbol{k})}{|n'(\boldsymbol{k})|}$.

In the main text of Fig. 2(f), we present the distribution of the measured eigenvector $n(\boldsymbol{k})$ in the whole Brillouin zone. Compared with the real-valued eigenstates vector obtained from the tight-binding model in Fig. 1(e), the measured acoustic eigenstates around Γ point are visibly different due to the lower excitation efficiency at low frequency especially close to zero frequency. We then check quantitative the azimuth and the elevation angles of the measured eigenvector and the calculated eigenvector along two special lines, the M-Γ-M lines [Fig. 2(g) and FIG. S-9(a)] and the M-K-Γ-K'-M lines [Fig. 2(h) and FIG. S-9(b)], for the sake of supplementary, as well as other four low symmetry directions, the M-M''-M lines [FIG. S-9(c)], the M-M'-M lines [FIG. S-9(d)], the M'-Γ-M' lines [FIG. S-9(e)] and M''-Γ-M'' [FIG. S-9(f)]. The consistency of between the experiments and theory confirm the winding of the eigenstates vector and the meron pattern in the acoustic Bloch wave functions for the topological Euler insulator phase. The slight deviation between theory and experiment is mainly due to the finite size of effect and inevitable manufacturing accuracy error for acoustic metamaterials.

H. Details of the acoustic edge dispersions measurement

To measure acoustic edge dispersions, we insert an acoustic source into a resonator in the middle of the zigzag (armchair) boundary and then detect the acoustic profile along the zigzag (armchair) edge. At some typical frequencies, the acoustic profiles along the zigzag edges are presented in FIG. S-10(b) and the armchair edges in FIG. S-10(c-d). Acoustic pressure profiles at

a few layers of resonators near the edge boundaries are measured in the experiments, which is found to be sufficient to extract the acoustic edge dispersions. After Fourier transformation along projected armchair or zigzag directions, we obtain acoustic edge dispersions in experiments.

In our investigation of zigzag edge states, we observed distinct behaviors in the response to acoustic pressure signals when comparing two band above the gap with a single bulk band below it. Two primary factors contribute to the observed deviations. One explanation for this is that the zigzag edge states are not well localized. They in fact spread a lot into the bulk. This means that the finite size effect is severer in our system than expected which is probably the main cause of the deviation. Another contributing factor to the deviations is the impact of finite size effects coupled with print errors inherent in the fabrication process. These imperfections exacerbate the influence of finite size effects. To address these challenges and extract both the bulk and zigzag edge dispersions simultaneously, we implement a dual measurement strategy. Firstly, we insert an acoustic microphone into a resonator in the middle of the zigzag boundary and then detect the acoustic profile along the zigzag edge. Acoustic profiles at a few layers of resonators near the edge boundary are measured in the experiment, which is found to be sufficient to extract the acoustic zigzag edge dispersions. After Fourier transformation along projected zigzag direction, we obtain the acoustic zigzag edge dispersions in experiments. Further to extract the projected bulk dispersion along zigzag direction, we insert the acoustic microphone into a resonator in the center of the experimental setup, and then manually one-by-one check the acoustic pressure amplitude and phase signals at each resonator. Performing the same measurement and Fourier transformations (date processing) as the same as first step, we obtain the acoustic projected bulk dispersion along zigzag direction. Through these meticulous efforts, we successfully retrieve both the upper bulk band and zigzag edge dispersions in our acoustic experiments. This comprehensive approach provides a nuanced understanding of the system's behavior, accounting for the challenges posed by finite size effects.

In the main text, we have presented the measured and calculated acoustic dispersions for the zigzag boundary in Fig. 2(d). Here, we present the measured and calculated acoustic dispersions for the armchair boundary in FIG. S-11(b). The armchair edge dispersions for the kagome TBM are also given in FIG. S-11(a). Although the acoustic band below the gap has trivial(zero) Berry phase, the topological edge states emerge in the gap due to the fact that the sites are located at the

unit-cell boundaries. Such gapped edge states firmly confirm the fragile topology of the second and the third bands.

In general, for the topological Euler phases studied here, which is a type of fragile topological phase protected by the C_2T symmetry, the system does not support robust gapless edge states. All the edge states studied in this work are associated with the Zak phase---it turns out that the odd Euler class phase in this work has nontrivial Zak phase (indicating a shifted location of the band Wannier states as compared to the atomic Wannier states) that can induce edge states. It is also known that such edge states are robust only when the system has the chiral symmetry (i.e., the combination of the time-reversal and the particle-hole symmetries). However, in our system, the TNN couplings (diagonal terms in the Hamiltonian) ruin the chiral symmetry, and the edge states are not robust. Nevertheless, the edge states can clearly be seen in the topological band gap for zigzag edges. For the armchair edges, we find that in the limit with vanishing TNN couplings, the armchair edge states appear in both gap-I and gap-II, due to the nontrivial Zak phase topology at any momentum projected to the armchair edge (see FIG. S-11(c) below). By increasing the TNN couplings, gap-I gradually evolves into a large complete band gap, whereas gap-II becomes a small partial band gap (see FIG. S-11(d)). As gap-II becomes smaller and smaller, the edge states in gap-II gradually shift into gap-I, as shown in FIG. S-11(b). This is possibly due to the energy shift induced by the TNN couplings (i.e., diagonal terms in the Hamiltonian) which is sensitive to the geometry of the edge boundary (i.e., more pronounced for the armchair edges).

For both zigzag and armchair edge dispersions, we find consistency between the calculated and measured edge dispersions. The slight deviations between the experimental date and theoretical curves are probably due to the geometry imperfection of the resonators near the edge boundaries in both samples due to uncontrollable fabrication errors.

I. Quadratic node and Dirac points

FIG. S-12 presents the dispersions of the quadratic nodes and Dirac points appearing between the second and the third bands for the case in Fig. 1(d) of the main text. Specifically, the dispersion of quadratic node at Γ point with patch Euler class of 1 is shown in FIG. S-12(a) (calculation) and FIG. S-12(d) (measurement). The dispersion of Dirac point at K point with Euler class of 1/2 is

shown in FIG. S-12(b) (calculation) and FIG. S-12(e) (measurement). The three M points exhibit quadratic nodes each of Euler class 1, shown in FIG. S-12(c) (calculation) and FIG. S-12(f) (measurement). We emphasize that the four quadratic nodes residing at Γ and M points are essentially a combination of a pair of Dirac points. They cannot be annihilated unless the bands above the gap close with the first band below the gap.

J. Effect of defect and robustness of zigzag edge states

In this section, we will investigate the localization of zigzag edge states and verify their robustness in numerical simulations. To this end, we hereby constitute a 2D-finite acoustic metamaterial with zigzag boundary. As shown in FIG. S-13(b), the system has zigzag left boundary with hard sound wall condition, while other three boundaries are half opened, so that acoustic wave can leak out into free space. We obtain the eigenfrequencies and according eigenstates of the system. As illustrated in FIG. S-13(a), the local zigzag edge states exist within the bulk gap. FIG. S-13(b) represents the spatial distribution of the sound pressure field at a characteristic frequency, which is localized predominantly in a few columns near the zigzag boundary. The strong localization of the zigzag edge state due to Euler class implies this state should be insensitive against defect in other sublattices.

To validate the robustness of the zigzag edge states in our metamaterial, we introduce two types of defects within blue solid regions: (1) modification of the heights of the cylinder sites to $H + \Delta H$ inside blue solid regions [Supplementary FIG. S-13(c-e)]; (2) modification of the radii of cylinder sites to $r_c + \Delta r_c$ inside blue solid regions [Supplementary FIG. S-13(f-h)]. Even a 10% shift in geometry paraments at metamaterial edges caused only a small frequency shift of no more than 2% for in-gap zigzag edge states. Notable, the zigzag edge states located furthest away from the bulk exbibits exceptional robustness, with a shift of no more than 10Hz [see in FIG. S-13(d, e, g, h)]. Additionally, the distributions of sound pressure fields still show excellent localization, compared with the zigzag edge state without defects in FIG. S-13(a). These results confirm the salient topology of gapped Euler phase, namely, the fragile topology of the second and the third bands.

K. References

[S-1] J. Zak, “Berry’s phase for energy bands in solids,” Phys. Rev. Lett. 62, 2747–2750 (1989).
[S-2] J. Zak, “Symmetry Specification of Bands in Solids,” Phys. Rev. Lett. 45, 1025–1028 (1980).
[S-3] J. Zak, “Band representations and symmetry types of bands in solids,” Phys. Rev. B 23, 2824–2835 (1981).
[S-4] L. Michel and J. Zak, “Connectivity of energy bands in crystals,” Phys. Rev. B 59, 5998–6001 (1999).
[S-5] L. Michel and J. Zak, “Elementary energy bands in crystalline solids,” EPL 50, 519 (2000).
[S-6] L. Michel and J. Zak, “Elementary energy bands in crystals are connected,” Phys. Rep. 341, 377 – 395 (2001), symmetry, invariants, topology.
[S-7] J. Höller and A. Alexandradinata, “Topological Bloch oscillations,” Phys. Rev. B 98, 024310 (2018).
[S-8] J. Zak, “Symmetry Specification of Bands in Solids,” Phys. Rev. Lett. 45, 1025–1028 (1980).
[S-9] A. P. Schnyder, S. Ryu, A. Furusaki, and A. W. W. Ludwig, “Classification of topological insulators and superconductors in three spatial dimensions,” Phys. Rev. B 78, 195125 (2008).
[S-10] A. Kitaev, “Periodic table for topological insulators and superconductors,” AIP Conf. Proc. 1134, 22 (2009).
[S-11] A. Hatcher, Vector Bundles and K-Theory (Unpublished, 2003).
[S-12] Y. X. Zhao and Y. Lu, “PT-Symmetric real Dirac Fermions and Semimetals,” Phys. Rev. Lett. 118, 056401 (2017).
[S-13] M. I. Aroyo, A. Kirov, C. Capillas, J. M. Perez-Mato, and H. Wondratschek, Acta Cryst. A 62, 115-129 (2006).

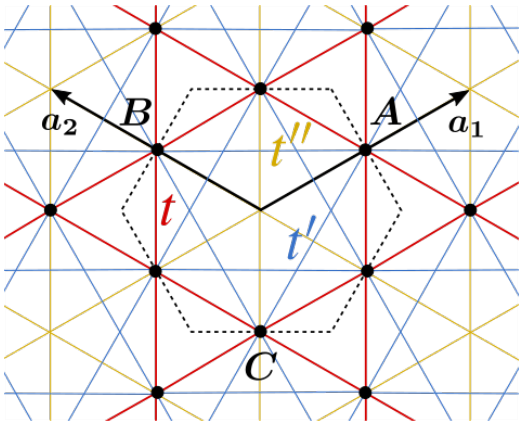


FIG. S-1. **Kagome lattice structure.** Kagome lattice (black dots). Red lines are the first-neighbor bonds of the kagome lattice with a tunneling amplitude written *t*. The blue (yellow) lines are the second (third) neighbor bonds with *t'*, and *t''*, respectively.

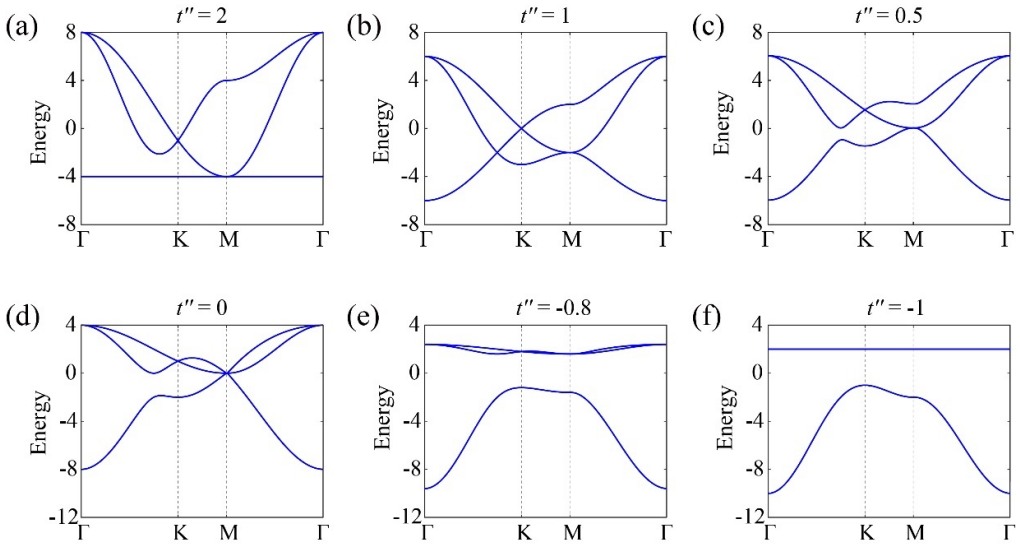


FIG. S-2. **The evolution of bulk energy spectra with the TNN coupling in the tight-binding model.** The NN and NNN couplings are fixed at negative unit and the strength of the TNN coupling is presented in the top of each panel. Continuously tuning the strength of TNN coupling, the three-band system is converted into Euler topological insulators phase (e-f) from non-Abelian semimetals phase (a-d).

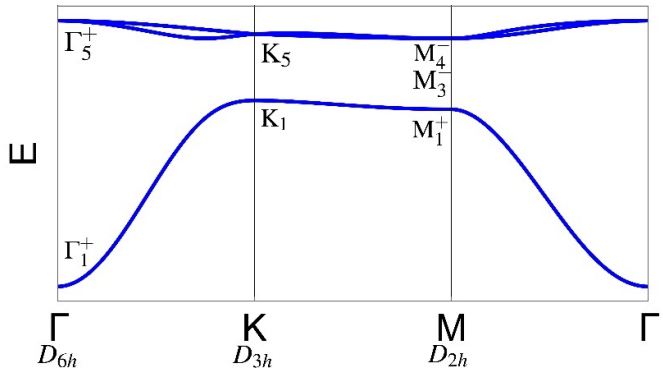


FIG. S-3. **Split elementary band representation (EBR) of the gapped kagome system.** We give the IRREPs for the symmetry group of the system (D_{6h}) (we use the convention of the Bilbao Crystallographic Server [S-13]). Below each high-symmetry points we have noted the corresponding little co-group.

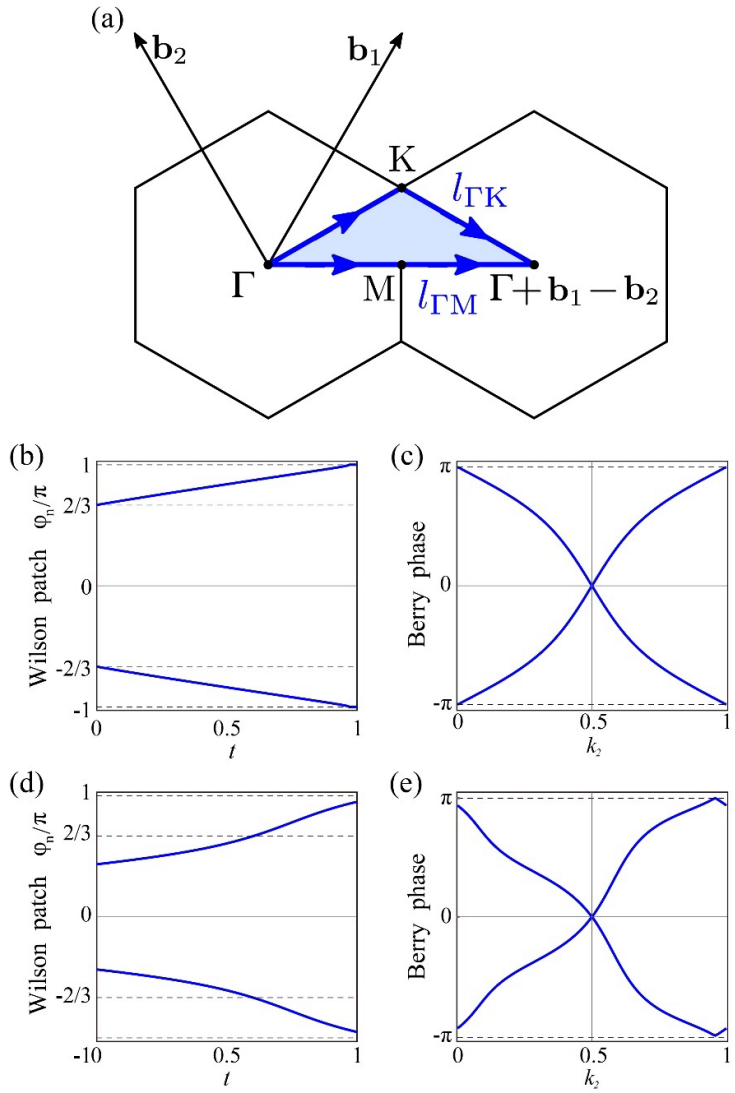


FIG. S-4. **Quantized Wilson loop indicating a fragile topological crystalline phase.** (a) Symmetric patch of the Brillouin zone (in blue) bounded by $l_{\Gamma K}$ and $l_{\Gamma M}$ over which we consider the flow of Wilson loop, by smoothly deforming $l_{\Gamma K}$ to $l_{\Gamma M}$. Considering the split EBR of FIG. S-3, the panel (b) shows the quantization of the winding of the two-band Wilson loop over the patch from $l_{\Gamma K}$ at $t = 0$ to $l_{\Gamma M}$ at $t = 1$ (See [67] for a detailed derivation). The panel (c) shows the resulting complete winding of the Wilson loop over the whole Brillouin zone, *i.e.* $6\left|\pi - \frac{2\pi}{3}\right| = 2\pi$, given that the patch covers one sixth of the Brillouin zone. (d) and (e) are the same as (b) and (c) but now with broken crystalline symmetries, while preserving C_2T (IT).

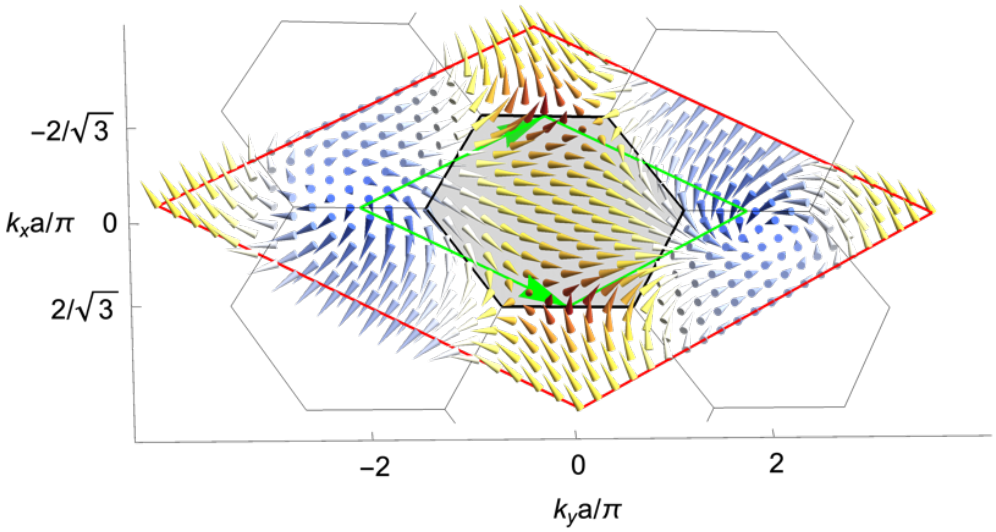
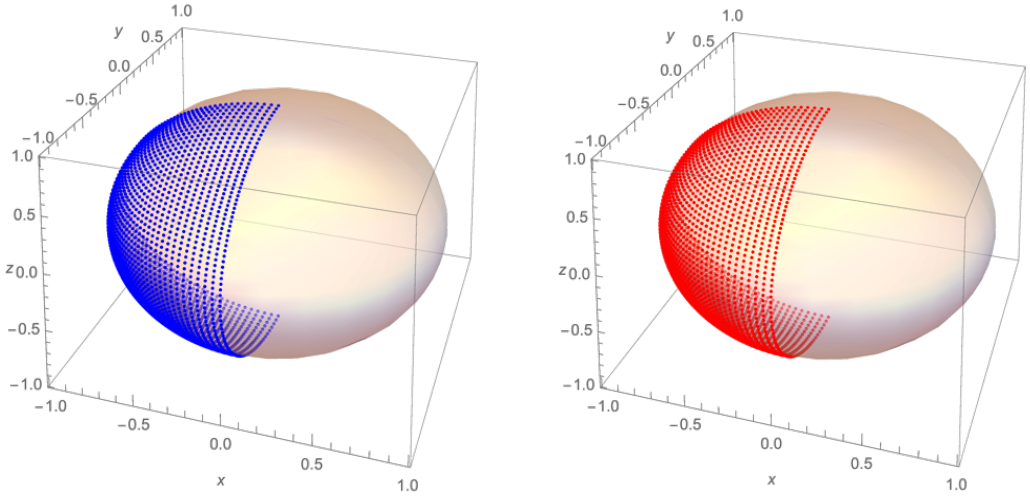


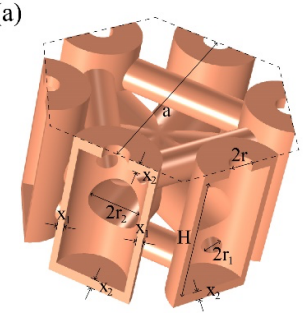
FIG. S-5. **Parallel transported vector field of $u_1(k)$ over four Brillouin zone (red rhombus).** While the vector field $u_1(\boldsymbol{k})$ is not periodic over a single Brillouin zone rhombus (green), it is periodic over four Brillouin zone (red rhombus). It is very clear that the large rhombus contains two Skyrmion windings, which implies a winding by half of a Skyrmion, that is a meron, in a single Brillouin zone (green).



(a) **(b)**

FIG. S-6. **Two parts separation of the vector field $\boldsymbol{u_1(k)}$ represented as points on the unit sphere.** The left panel (blue dots) represents $\boldsymbol{u_1(k)}$ for $k_1 \in [-0.5, 0.]$ and $k_2 \in [-0.5, 0.5]$, and the right panel (in red) represents $\boldsymbol{u_1(k)}$ for $k_1 \in [0., 0.5]$ and $k_2 \in [-0.5, 0.5]$. This is a result of the inversion symmetry of the vector field, i.e. $\boldsymbol{u_1(-k) = u_1(k)}$. We use this relation to prove that the total vector field $\boldsymbol{u_1(k)}$ generates a meron winding number. Crucially, each part covers exactly one half of an hemisphere.

(a)



(b)

Variable	Explanation	Dimension in [mm]
a	lattice constant	$36\sqrt{3}$
H	height of resonators	36
r_c	radii of resonators	9.6
r_1	radii of NNN coupling tubes	2.7
r_2	radii of TNN coupling tubes	7
x_1	resin thickness of each tube and each resonators	1.8
x_2	resin thickness of top and bottom layers	3
r	radii of hole in top layer	3.5

FIG. S-7. **The designed unit-cell structure.** (a) The unit-cell of one of the designed kagome acoustic metamaterial. Cylindrical acoustic resonators are located at the centers of unit-cell boundaries (because of the periodicity of the structure, half cylinders are shown in the figure). The orange regions represent the photosensitive resin which is used in the 3D printing technology to fabricate the acoustic metamaterials. Horizontal tubes are used to connect the resonators in order to realize the NN, NNN and TNN couplings. (b) The geometry parameters of the kagome acoustic metamaterial.

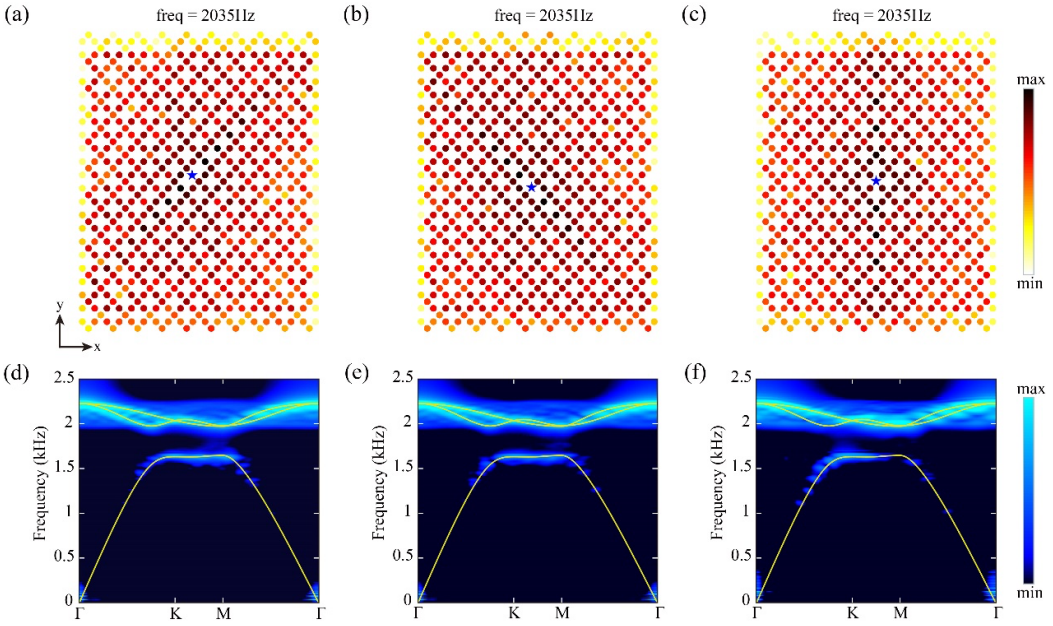


FIG. S-8. (a-c) Experimental measurements of acoustic pressure profiles in the bulk. The excitation frequency, at a typical frequency 2035HZ, is labeled in the title of each figure. The reversal hot colormap represents the amplitude of measured acoustic pressure. And the acoustic sources are also highlighted by blue stars. (d-f) Experimental measurements of acoustic bulk band structures along high symmetry lines Γ-K-M-Γ. The color scheme gives the amplitude of the measured acoustic signals after Fourier transformation (linked to the acoustic band structures), while the yellow lines represent the calculated acoustic band structures. The left, middle and right columns correspond to the cases with the acoustic source placed at the A, B and C sites, respectively. FIG. S-8(d) is selected into Fig. 2(c) in the main text.

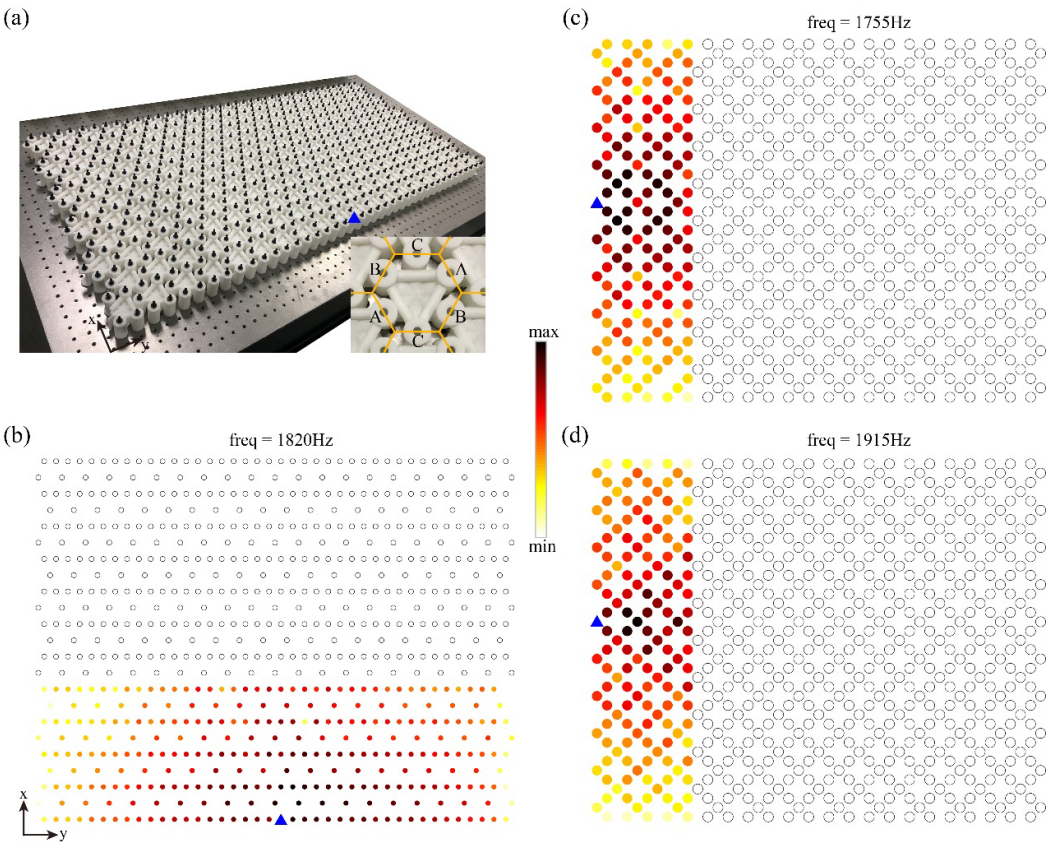


FIG. S-10. **Observation of topological edge states in finite-sized acoustic metamaterials.** (a) Photograph of the fabricated acoustic metamaterial for acoustic armchair edge dispersions measurement. The blue triangle denotes the acoustic source for excitation of armchair edge states. Inset: zoom-in photograph of the metamaterial, with orange lines depicting the boundaries of the unit cells. (b) The measured acoustic pressure profiles along the zigzag edge when the source (labeled by the blue triangle) is placed at the middle of zigzag boundary. (c-d) The measured acoustic pressure profiles along the armchair edge when the source (labeled by the blue triangle in each figure) is placed at the middle of armchair boundary. The excitation frequency of source is given at the top of figure. Acoustic pressure profiles at a few layers of resonators near the edge boundaries are measured in the experiments, which is found to be sufficient to extract the acoustic edge dispersions.

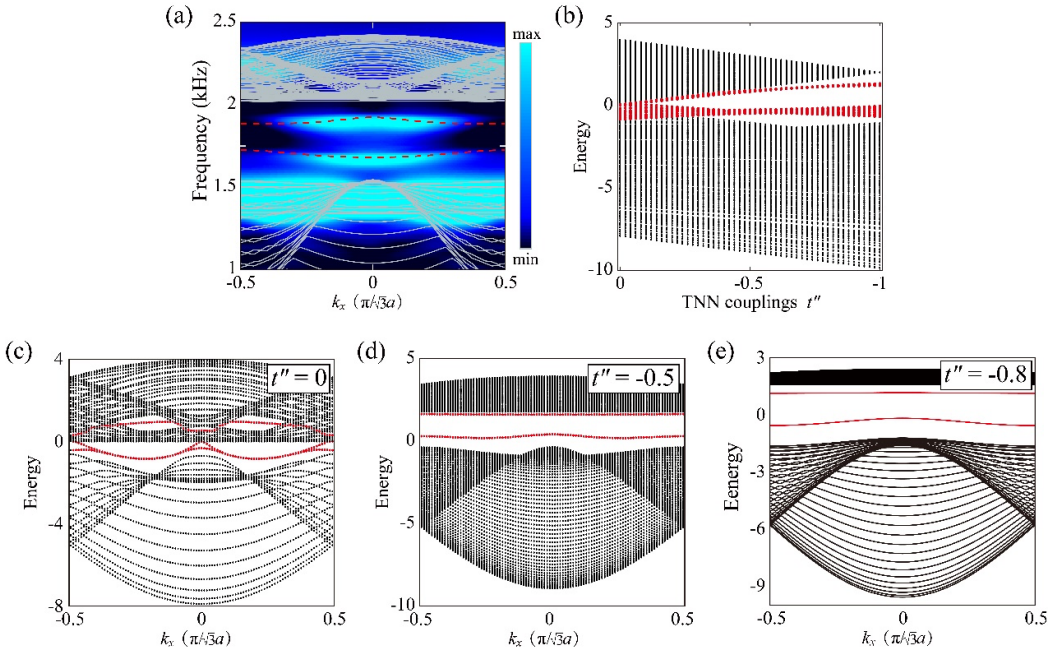


FIG. S-11. **Armchair edge states in Euler insulators phase.** (a) Measured (color map) and simulated (red dashed curves) dispersions of the acoustic armchair edge states. Gray curves represent simulated bulk bands projected to the armchair edge. (b) The evolutions of the armchair edge states with the TNN couplings. (c) Without the TNN couplings, one branch of the armchair edge states appears in gap-I, while another branch appears in gap-II. (d-e) By increasing the TNN couplings, the armchair edge states in gap-II gradually evolves into gap-I. In the TBM, we set the NN and NNN couplings equal to -1. The edge states are highlighted by red dotted lines.

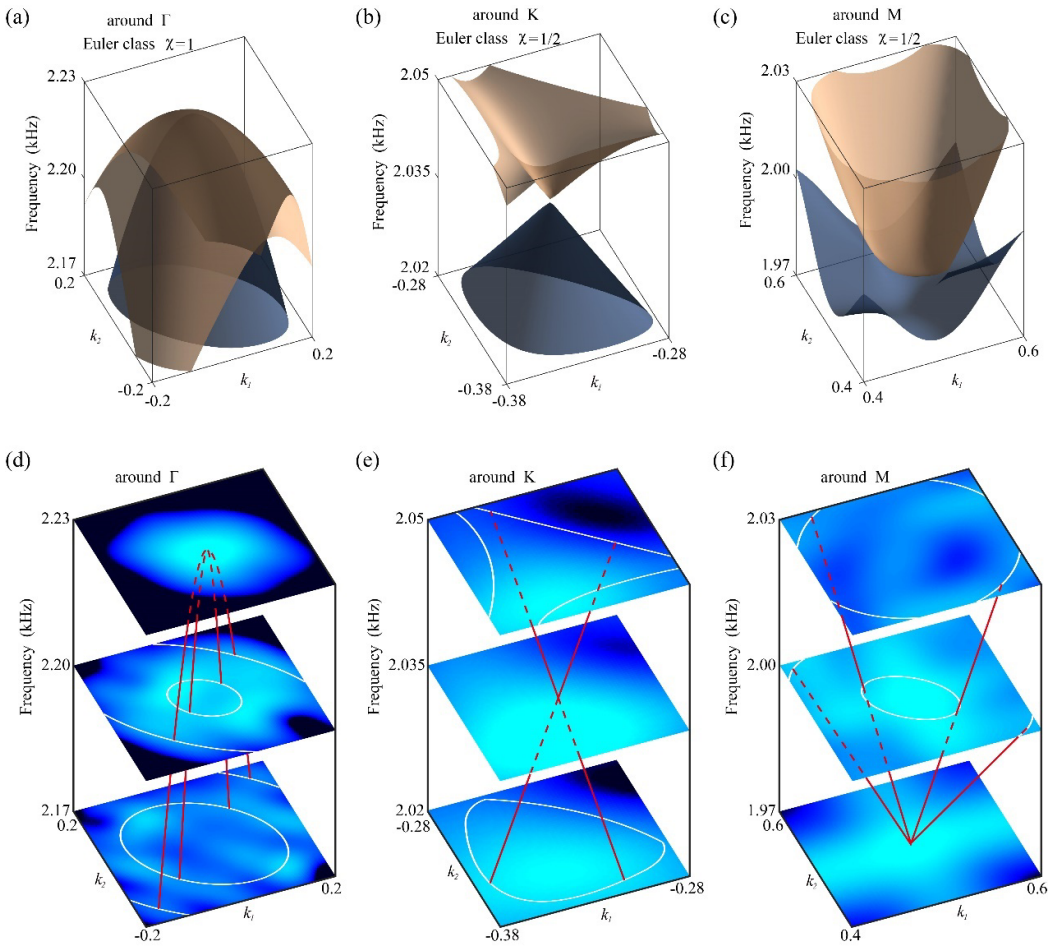


FIG. S-12. **Dispersions of quadratic node and Dirac points in the second and the third bands for the case in Fig. 1(d).** (a, d) Calculated (a) and Measured (d) acoustic dispersions around the Quadratic node at the Γ point. (b, e) Calculated (b) and Measured (e) acoustic dispersions around the Dirac point at the K point. (c, f) Calculated (c) and Measured (f) acoustic dispersions around the Dirac point at the M point. In (a-c), the color surfaces represent the dispersions. In (d-f), iso-frequency contours represent the dispersions. White solid lines represent calculated iso-frequency contours, while the red lines are guide to the eye to illustrate the dispersions from calculations. k_1 and k_2 are the wavevectors along reciprocal primitive vectors.

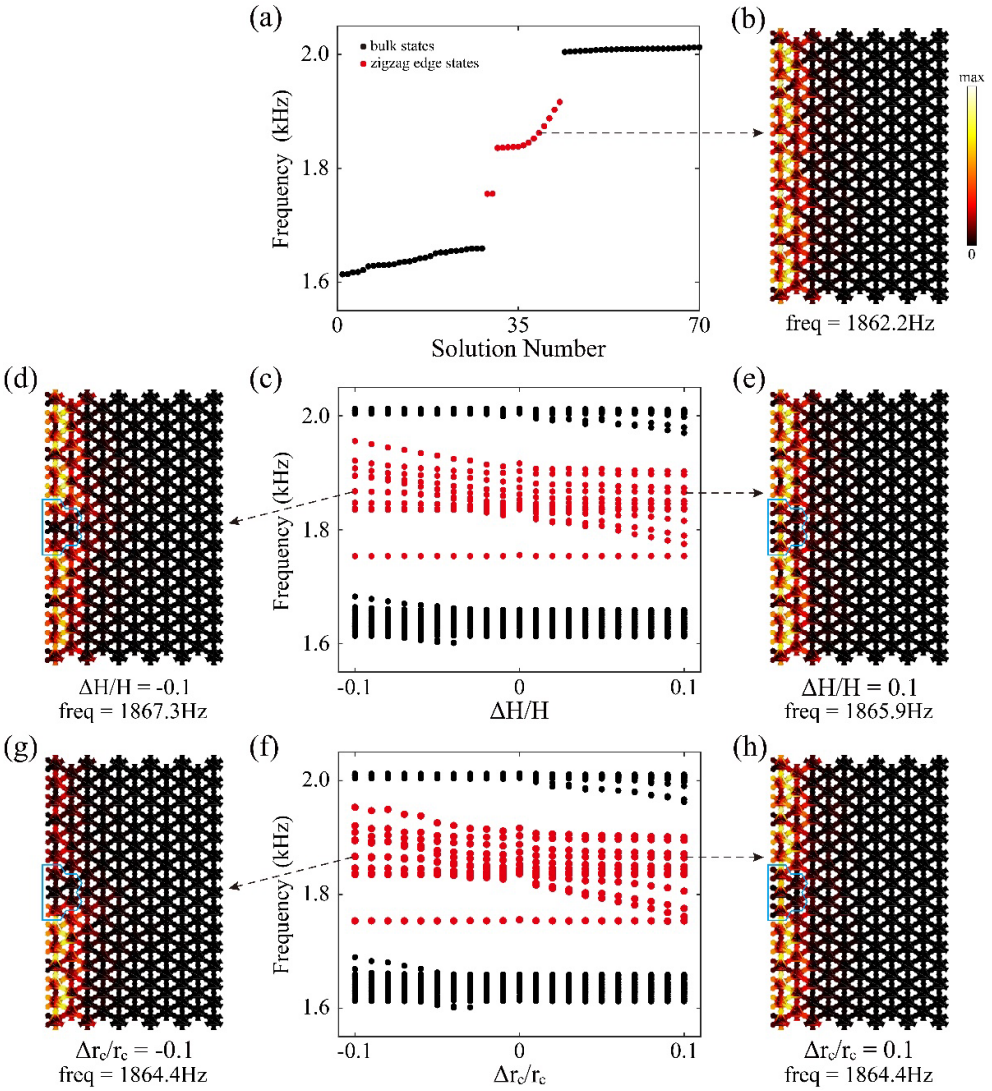


FIG. S-13. **Zigzag edge states, effect of defect and the robustness of zigzag edge states.** (a) Simulation results of eigenfrequencies in a 2D finite acoustical metamaterial. Red dots represent zigzag edges states, and black dots represent bulk states. (b) Absolution value of distribution of acoustic pressure field at frequency 1862.2Hz. Bright (Black) color represents strong(weak) acoustic pressure field. (c-e) In the presence of defect in blue solid regions, we slightly modify the heights of cylinder sites to $H + \Delta H$. The numerical simulations of eigenfrequencies are presented in panel (c), and the distributions of acoustic pressure fields are presented in panel (d, e). (f-h) In the presence of defect in blue solid regions, we slightly modify the radii of cylinder sites to $r_c + \Delta r_c$. The numerical simulations of eigenfrequencies are presented in panel (f), and the distributions of acoustic pressure fields are presented in panel (g, h).